Article

Cell

Rare Pulmonary Neuroendocrine Cells Are Stem Cells Regulated by Rb, p53, and Notch

Graphical Abstract

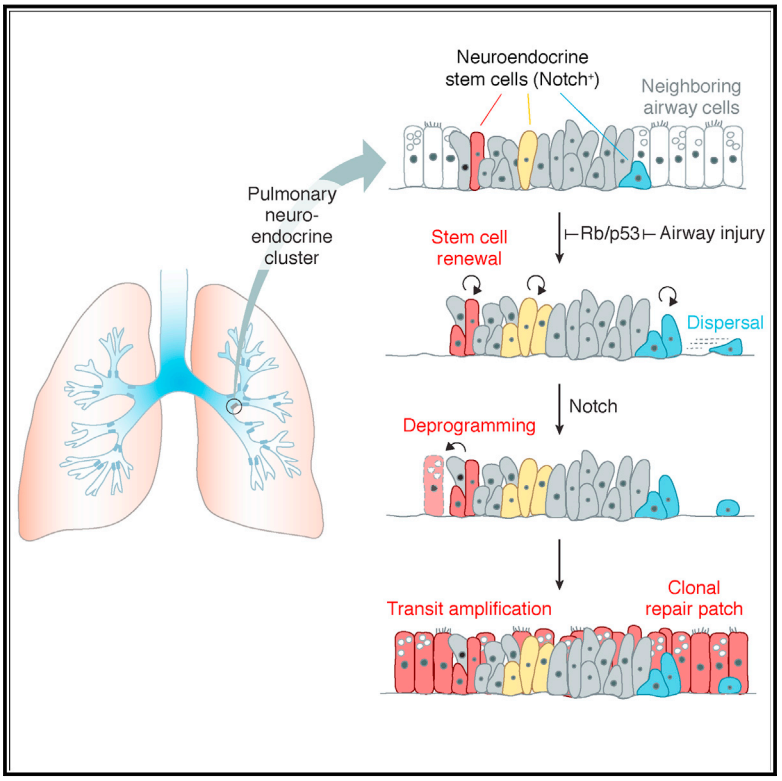

Highlights

- Rare, fully differentiated neuroendocrine cells are stem cells activated by injury
- Injury induces stem cell renewal, dispersal, transit amplification, and reprogramming
- Tumor suppressors Rb, p53, and Notch control specific steps in stem cell program
- Small-cell lung cancer arises by genetic activation of stem cell renewal and dispersal

Authors

Youcef Ouadah, Enrique R. Rojas, Daniel P. Riordan, Sarah Capostagno, Christin S. Kuo, Mark A. Krasnow

Correspondence

krasnow@stanford.edu

In Brief

A small fraction of differentiated neuroendocrine cells possesses the ability to act as reserve stem cells during lung injury.

Ouadah et al., 2019, Cell *179*, 403–416
October 3, 2019
https://doi.org/10.1016/j.cell.2019.09.010

CellPress

Cell

Rare Pulmonary Neuroendocrine Cells Are Stem Cells Regulated by Rb, p53, and Notch

Youcef Ouadah,[1,2,6] Enrique R. Rojas,[1,3,7] Daniel P. Riordan,[1,8] Sarah Capostagno,[5] Christin S. Kuo,[4] and Mark A. Krasnow[1,9,*]

[1]Department of Biochemistry and Howard Hughes Medical Institute, Stanford University School of Medicine, Stanford, CA 94305, USA
[2]Program in Cancer Biology, Stanford University School of Medicine, Stanford, CA 94305, USA
[3]Department of Bioengineering, Stanford University School of Medicine, Stanford, CA 94305, USA
[4]Department of Pediatrics, Division of Pulmonary Medicine, Stanford University School of Medicine, Stanford, CA 94305, USA
[5]Department of Biomedical Engineering, Johns Hopkins University, Baltimore, MD 21205, USA
[6]Present address: Caltech Division of Biology and Biological Engineering, Pasadena, CA 91125, USA
[7]Present address: NYU Department of Biology, New York, NY 10003, USA
[8]Present address: 10x Genomics, Inc., Pleasanton, CA 94566, USA
[9]Lead Contact
*Correspondence: krasnow@stanford.edu
https://doi.org/10.1016/j.cell.2019.09.010

SUMMARY

Pulmonary neuroendocrine (NE) cells are neurosensory cells sparsely distributed throughout the bronchial epithelium, many in innervated clusters of 20–30 cells. Following lung injury, NE cells proliferate and generate other cell types to promote epithelial repair. Here, we show that only rare NE cells, typically 2–4 per cluster, function as stem cells. These fully differentiated cells display features of classical stem cells. Most proliferate (self-renew) following injury, and some migrate into the injured area. A week later, individual cells, often just one per cluster, lose NE identity (deprogram), transit amplify, and reprogram to other fates, creating large clonal repair patches. Small cell lung cancer (SCLC) tumor suppressors regulate the stem cells: Rb and p53 suppress self-renewal, whereas Notch marks the stem cells and initiates deprogramming and transit amplification. We propose that NE stem cells give rise to SCLC, and transformation results from constitutive activation of stem cell renewal and inhibition of deprogramming.

INTRODUCTION

Most of the remarkable progress in adult stem cell biology over the past few decades has focused on "professional" stem cells—immature cells with dedicated stem cell function—such as those in high turnover tissues including bone marrow, gut, and skin (Morrison and Spradling, 2008; Potten and Loeffler, 1990). More recently, it has become clear other tissues, especially low turnover tissues like lung, liver, and pancreas, are maintained at least in part by differentiated cells with physiological as well as stem cell functions (Clevers and Watt, 2018; Logan and Desai, 2015). These cells are not terminally differentiated as once thought, but can reenter cell cycle and generate daughters that reprogram (transdifferentiate) to other fates (Merrell and Stanger, 2016). An early and striking example was pulmonary neuroendocrine (NE) cells (Stevens et al., 1997).

Pulmonary NE cells are specialized sensory cells that monitor airway status and signal to other lung cells and to the brain through synapses with sensory neurons (Cutz et al., 2013; Garg et al., 2019). Although they have many functions and features of sensory neurons, NE cells are considered neuroepithelial because they are embedded in the bronchial epithelium and share junctions and polarized structure with neighboring epithelial cells, including multiciliated and club cells (Adriaensen and Scheuermann, 1993). Indeed, they arise from common bronchial progenitors that undergo a transient epithelial-mesenchymal transition as they migrate ("slither") toward airway branch points, where they form clusters of ~20–30 NE cells termed neuroepithelial bodies (NEBs) (Kuo and Krasnow, 2015; Noguchi et al., 2015).

NE cells normally divide rarely, if ever (Boers et al., 1996). However, following extensive epithelial injury by the club cell toxicant naphthalene (Stevens et al., 1997) or genetic ablation of club cells (Reynolds et al., 2000), NE cells proliferate and repair the surrounding epithelium (Song et al., 2012). Their proliferative potential has also been demonstrated by their oncogenic transformation following deletion of tumor suppressors *Rb1* and *Trp53* in mice (called *Rb* and *p53* here) (Park et al., 2011a; Song et al., 2012; Sutherland et al., 2011), which are universally inactivated in small cell lung cancer (SCLC) (George et al., 2015). Indeed, NE cells are the proposed cell of origin for SCLC, which comprises 15% of lung cancer cases and is the most deadly form (Semenova et al., 2015).

Here, we probe NE stem cell function at single-cell resolution in mouse lung and show only a minor subpopulation of differentiated NE cells has stem cell function. We map the cellular events of the stem cell program and their regulation by SCLC tumor suppressors and identify *Notch2* as a stem cell marker. The results suggest these stem cells are tumor-initiating cells in SCLC, and transformation results from permanent activation of early steps in the stem cell program.

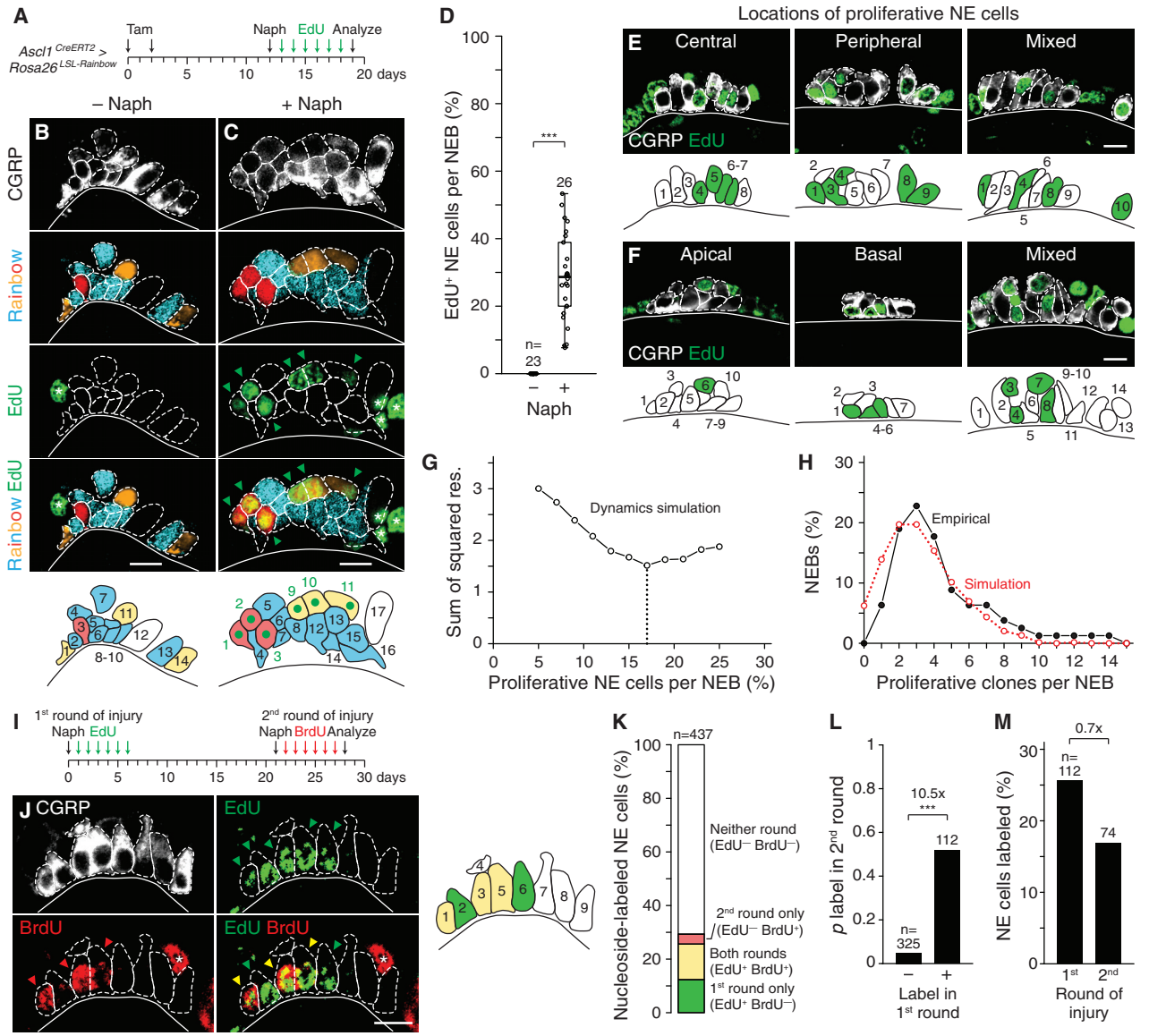

Figure 1. A Subpopulation of NE Cells Proliferates after Airway Injury

(A) Cumulative proliferation tracing of individual Ascl1$^+$ pulmonary NE cells in adult mice. Tamoxifen (Tam) induces Cre recombination and stochastically labels NE cells with one of three Rainbow fluorescent proteins. Naphthalene (Naph) ablates club cells, and nucleoside analog EdU identifies cells that proliferate.

(B and C) Optical sections showing EdU incorporation in mock-injured (B, NEB9 Table S1) or naphthalene-injured (C, NEB31), Rainbow-labeled NEBs analyzed by immunostaining (NE marker CGRP) and click chemistry (EdU). Dashed outlines, individual NE cells (numbered in schematics) identified by CGRP and Rainbow reporter expression. After injury (C), EdU incorporated in two NE clones (cells 1–3, 9–11). Green arrowheads (dots in schematic), EdU$^+$ NE cells; asterisks, EdU$^+$ non-NE cells. Note that NE cells undergo hypertrophy after naphthalene injury (Peake et al., 2000).

(D) Quantification (box-and-whisker plots) of (B) and (C) showing median, interquartile range (IQR), and range of data points within 1.5 × IQR. Median values, 0, 29%; n, NEBs scored, 2 control, 3 naph mice; ***$p < 10^{-9}$, two-sided Mann-Whitney U test.

(E and F) Positions of proliferative (EdU$^+$) NE cells in NEBs. Note diffuse distribution across lateral (E) and apicobasal (F) planes.

(G) Dynamics simulation showing best fit (dotted line, 17%) to experimental data given optimal values of cell division rate (0.0003 h^{-1}) and proliferative period (45 h).

(H) Relative frequency distribution of proliferative clones per NEB determined empirically (black, maximal value possible) from EdU and Rainbow labeling (Table S1), along with dynamics simulation (red) assuming 17% of NE cells can proliferate. Most NEBs contain 2–4 proliferative clones.

(I) Independent tracing of NE cell proliferation after sequential injuries (EdU, first injury round; BrdU, second round).

(J) Optical section of NEB (NEB51 Table S2) sequentially injured then immunostained (CGRP, BrdU) and click chemistry for EdU. Dashed outlines, NE cells; arrowheads, EdU$^+$ (green), BrdU$^+$ (red), and EdU$^+$ BrdU$^+$ NE cells (yellow); asterisk, BrdU$^+$ non-NE cell. All three NE cells that proliferated following second injury (BrdU$^+$) had also proliferated following first (EdU$^+$).

(legend continued on next page)

RESULTS

A Subpopulation of NE Cells Has Stem Cell Activity

To determine the number of NE cells in each NEB that proliferate after airway injury, we genetically labeled individual NE cells with different fluorescent proteins using a NE-specific Cre driver (*Ascl1*^{CreERT2}) (Kim et al., 2011; Kuo and Krasnow, 2015) bred to a multicolor Cre reporter (*Rosa26*$^{LSL\text{-}Rainbow}$) (Rinkevich et al., 2011) (Figures S1A–S1D). We then ablated club cells with naphthalene and tracked proliferation by daily injection of thymidine analog ethynyldeoxyuridine (EdU) (Figure 1A). NE cells were quiescent before injury and proliferated after, as expected (Figures 1B–1D; Table S1). However, even at the highest naphthalene doses compatible with survival (275 mg/kg), which ablate nearly all (~95%) club cells (Reynolds et al., 2004), only 29% of NE cells (8/NEB) incorporated EdU during the first week following injury (Figures 1C, 1D, and S1E). This resulted in a modest (20%) increase in median NEB size, from 23 to 28 NE cells (Figure S1E). In most NEBs that proliferated (81%), the EdU-positive population comprised at least two fluorescent labels (Figure 1C; Table S1), indicating multiple parental cells proliferated. Indeed, the clonal distribution (Figure S1F) and dynamics simulations (Figure S1G) indicate 2–4 NE cells per NEB (mode 3, 17% of parental cells) proliferate, each generating 1–3 additional NE daughter cells (Figures 1G, 1H, and S1H–S1L). Cells that proliferated were scattered throughout NEBs (Figures 1E and 1F).

To determine if the cells that proliferate on injury are a dedicated stem cell population, or simply the result of stochastic activation of NE cells, we injured mice with a second round of naphthalene three weeks later and tracked proliferation in this round with bromodeoxyuridine (BrdU) (Figure 1I). We reasoned if proliferating NE cells from the first round represent a dedicated subpopulation, they should selectively proliferate again in the second round. If instead all NE cells are equivalent in stem cell function, there should be no bias. We found substantial (10-fold) bias between injuries (Figures 1J–1L; Table S2), supporting a dedicated stem cell population: of the NE cells that proliferated after the second injury (BrdU-positive, 17% total NE cells), the majority (78%) had also proliferated after the initial injury (EdU/BrdU double-positive) despite their numerical minority (26% total NE cells EdU-positive). Only 4% of NE cells proliferated exclusively after the second injury. Similar results (5-fold bias) obtained using Ki67 immunostaining to identify actively proliferating NE cells in the second round (Figures S1M–S1P; Table S2). We conclude that a minor subpopulation of NE cells (~2–4/NEB), which we designate "NE^{stem}," has proliferative function, and many of them are activated in the first injury round but less in the second (Figures 1M and S1Q), the decline due at least in part to acquired resistance of club cells to naphthalene (O'Brien et al., 1989).

Some NE Cells Disperse after Injury

To examine the behavior of individual NE progenitors in repair, we used multicolor labeling as above with whole-mount immunostaining to visualize the 3D distribution of progenitors. We found that, in addition to small growth of NEBs from NE^{stem} proliferation, some NEBs (15%) also expanded by loosening or loss of contacts among NE cells in the parental cluster (Figures 2A–2C). Sometimes a small group of cells fragmented from the main cluster (Figure 2B). In other cases, a few cells (range 2–11, mode 3) dispersed individually, forming satellite cells located tens to hundreds of microns from the NEB (Figures 2B, 2D, and 2E). Dispersing cells were observed with migratory morphologies resembling "slithering" NE progenitors that coalesce into NEBs during development (Kuo and Krasnow, 2015; Noguchi et al., 2015) (Figure 2B). Dispersal occurred in the first week after injury, the same period as self-renewal, although EdU studies indicated not all dispersed cells had proliferated (Figure 2F). Thus, injury induces proliferation as well as rare, outward migrations of individual NE cells into the injured region.

A Single NE Cell Generates a Clonal Outgrowth that Restores Surrounding Epithelium

A week after injury, NE proliferation and dispersal ceased, and NE cells returned to quiescence (Song et al., 2012) (see Figure 6 below). During this period, all lineage-labeled NE cells (n = 563) continued to express calcitonin gene-related peptide (CGRP) (Figures 3A–3C and 3G), indicating NE^{stem} proliferation was exclusively self-renewal that generated additional NE cells but did not repair surrounding epithelium. However, over the next 2 weeks, some lineage-labeled cells proliferated to colonize the adjacent region, forming large patches of regenerated epithelium contiguous with and in most cases completely surrounding the parental NEB that together restored ~4% of the bronchial surface (Figures 3D, 3E, 3G, S2A–S2D, and S2F). The outgrowths were readily distinguished from earlier self-renewal events because, although the cells expressed the NE lineage label (albeit somewhat diluted by continuous proliferation), they did not express CGRP, indicating they had lost NE identity ("deprogrammed").

NE outgrowths were almost always monoclonal (81% of cases), composed of cells expressing the same Rainbow fluorophore (Figures 3D, 3E, and 3H). This indicates outgrowths typically arise by proliferation of a single "transit amplifying" cell (Potten and Loeffler, 1990) from the parental NEB that generates many cells (range 17–2,300, median 237) over 2 weeks (Figure 3G). Clones were coherent, with little or no intermixing of cells from other sources. Even in the uncommon cases (19% of outgrowths) when two cells in a NEB amplified to form biclonal outgrowths (Figures 3F and 3H), each clone remained segregated in its own territory separated by a clean boundary between them (Figure 3F). Thus, although NE outgrowths seamlessly restore the injured epithelium surrounding the NEB to its original

(K) Quantification of (J) showing distribution of CGRP^{+} NE cells that proliferated. n, cells scored, 13 NEBs, 4 mice.
(L) Derived probability (p) of NE cell proliferating after second injury stratified by whether it proliferated after first. n, cells scored; ***$p < 10^{-25}$, hypergeometric test of EdU/BrdU overlap in (K).
(M) Percent NE cells that proliferated after sequential injuries. n, cells scored. Bars, 10 μm.
See also Figure S1.

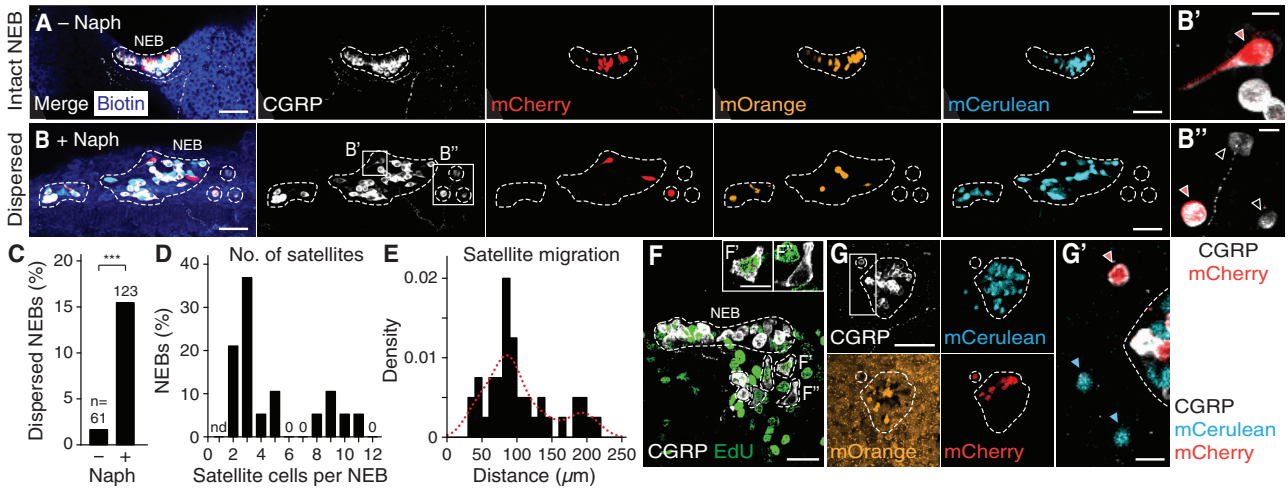

Figure 2. NE Cell Dispersal after Injury

(A–B″) Maximum intensity projections of Rainbow-labeled NEBs as in Figure 1A from mock- (A) or naphthalene-injured (B) mice analyzed 1 week later by CGRP staining (dashed outlines) and biotin counterstain (airway epithelium) of thick lung sections. Note expansion/fragmentation of NEB after injury and migratory morphology (B′, CGRP/mCherry overlay of boxed region) and dispersal of NE cells to form satellites (B″, CGRP/mCherry overlay). Red arrowheads, CGRP$^+$ mCherry$^+$ NE cells; open arrowheads, CGRP$^+$ mCherry$^-$ satellite cells.

(C–E) Quantification of frequency of dispersed NEBs (C, ***$p < 10^{-12}$, two-sided binomial test; n, NEBs scored, 2 control, 4 naph mice), satellite cells (D, n = 19 NEBs, 4 mice), and distance migrated from NEB center (E, red, kernel density fit; n = 40 satellite cells, 8 NEBs, 3 mice).

(F–F″) Maximum intensity projection of fragmented NEB (outlined) 1 week after injury, with EdU delivered daily to identify cells that proliferated and CGRP staining to identify NEBs and dispersed NE cells. Some (F′) but not all (F″) satellite cells proliferated.

(G) Dispersed NEB 3 weeks after injury showing mCherry$^+$ and mCerulean$^+$ satellite cells surrounded by newly regenerated airway cells from clonal expansion of mOrange$^+$ NE cell (see Figure 3). Dashed outline, NEB boundary and nearby mCherry$^+$ satellite NE cell.

(G′) Boxed region showing CGRP$^+$ mCherry$^+$ (red arrowhead) and two mCerulean$^+$ satellite cells (cyan arrowheads). Both mCerulean$^+$ cells are CGRP$^-$ and hence had deprogrammed NE identity but did not clonally expand. Bars, 50 μm (A, B and G), 25 μm (F), 10 μm (B′, B″, F′, F″, and G′).

state with appropriate cell types (Figures S2G and S2H), typically just a single cell participates in repair and its daughters retain a lineage memory that prevents intermixing with cells from other sources. The only observed exception was satellite cells, which were occasionally found within expanded clones (Figure 2G).

Single-Cell mRNA Sequencing Reveals Notch-Active NE Cells Undergoing Reprogramming

To identify genes that regulate these stem cell behaviors, we expression-profiled NE cells by single-cell RNA sequencing (scRNA-seq). Because they are rare (Boers et al., 1996), we lineage-labeled adult NE cells *in vivo* by tamoxifen induction of mice carrying *Ascl1*^{CreERT2} or *CGRP*^{CreERT2} (Song et al., 2012) drivers and *Rosa26*$^{LSL\text{-}ZsGreen}$ reporter (Madisen et al., 2010) and then used flow sorting to purify labeled NE cells and control unlabeled epithelial cells for mRNA amplification and scRNA-seq using a microfluidic system (Fluidigm C_1) (Treutlein et al., 2014) (Figures S3A–S3D).

T-distributed stochastic neighbor embedding (t-SNE) clustering using RaceID2 (Grün et al., 2016) of the expression profiles of the 225 cells that passed quality controls identified five principal cell clusters, which we identified by canonical markers as NE, multiciliated, club, alveolar type 2 (AT2), and stromal cells (Figures 4A and S3E; Table S3). Almost all the NE lineage-labeled cells (95 of 100) grouped together in the NE cluster, as expected (Figure 4A). However, five clustered with other cell types: 2 with club, 1 with multiciliated, 1 with AT2, and 1 with stromal cells, indicating they partly or fully reprogrammed to these fates after NE lineage labeling. These same five cells, plus three additional NE lineage-labeled cells, also separated from bulk NE cells when analyzed by principal component analysis (PCA) using overdispersed genes (Figure 4B). Highly loaded genes in the first two components (Figure S3F) revealed these 8 cells were "transitional" cells exhibiting downregulation of NE marker *Resp18* and upregulation of pan-lung epithelial marker *Cbr2* (Guha et al., 2014) (Figures 4B and S3E), suggesting they were actively undergoing reprogramming. Correlating expression of other genes to *Cbr2* identified *Hes1*, the canonical Notch pathway transcription factor (Jarriault et al., 1995) (Figure S3G). Indeed, *Hes1* was expressed in almost all transitional cells (7 of 8, 88%) but rarely in other NE cells (2 of 92, 2%) (Figures 4B and S3H), indicating Notch pathway was specifically activated in transitional cells. PCA of 160 additional *Ascl1*^{CreERT2} lineage-labeled and flow-sorted NE cells profiled by scRNA-seq in plate format identified a similar small set of Notch-active (*Hes1*-expressing) transitional cells (Figure S3J).

Notch signaling controls a wide variety of cell fate selections (Artavanis-Tsakonas et al., 1999), including in the bronchial epithelium during development and homeostasis (Hogan et al., 2014; Lafkas et al., 2015; Pardo-Saganta et al., 2015). Indeed, in addition to *Resp18* the 8 Notch-active transitional cells exhibited downregulation of a suite of NE markers (Figure S3I) and upregulation of markers of other pulmonary fates including club (e.g., *Scgb3a2*; 2/8), multiciliated (*Myb*, *Foxj1*; 3/8), alveolar

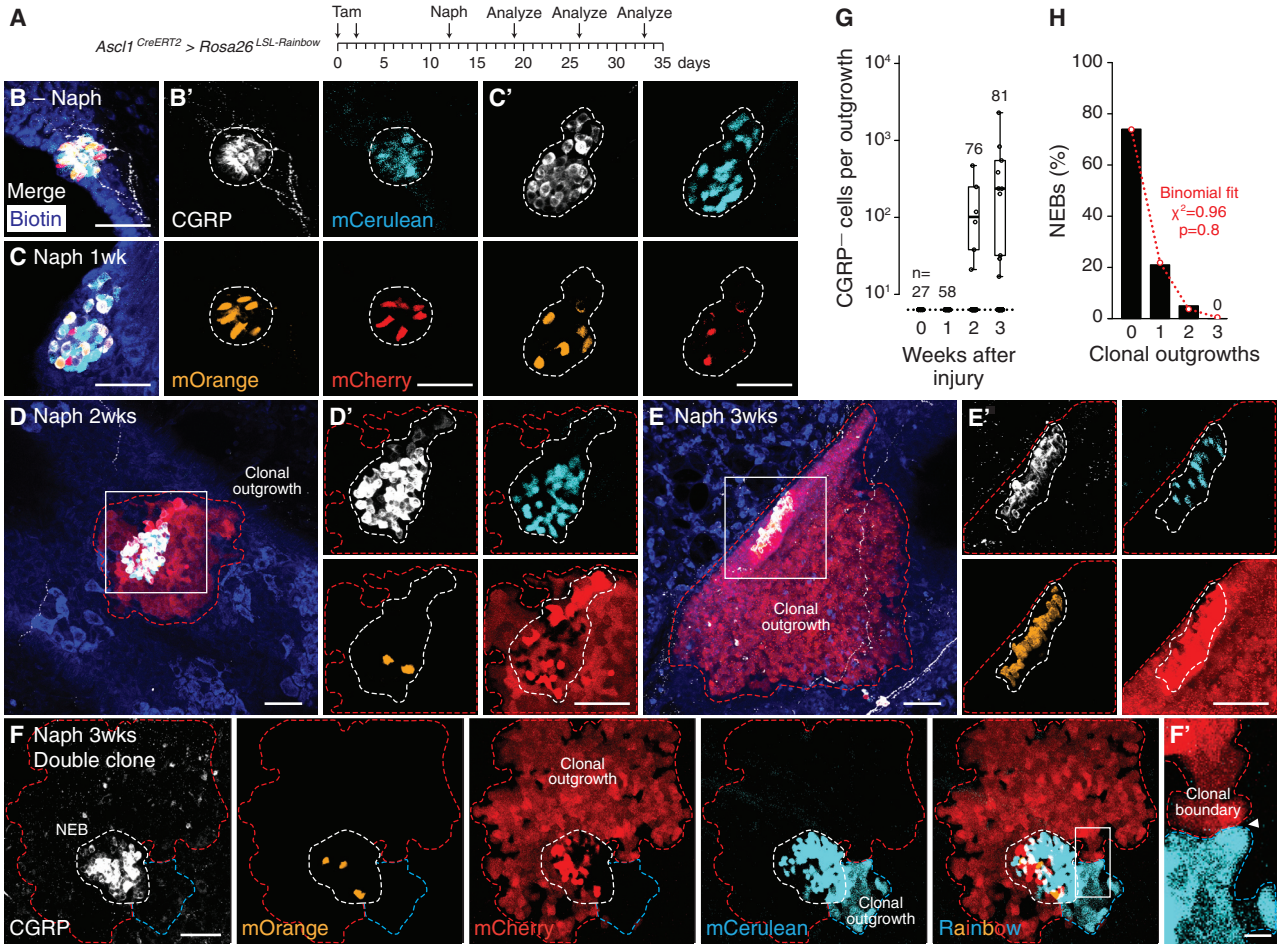

Figure 3. NE Reprogramming Generates Clonal Outgrowths

(A) Tracing NE cell dynamics and reprogramming at clonal resolution after injury.

(B–E′) Maximum intensity projections of CGRP-stained NEBs with Rainbow-labeled NE cells from mock- (B, split channels B′) or naphthalene-injured mice 1 (C, split channels C′), 2 (D, boxed region D′), and 3 weeks (E, boxed region E′) after injury. Blue, biotin counterstain (epithelium); white dashed outlines, NEBs (identified by CGRP staining); colored dashed outlines (D, E), NEB clonal outgrowths identified by Rainbow fluorophores. Note no NEB outgrowths (all Rainbow-labeled NE cells remain CGRP^{+}) 1 week after injury (C), but at 2 (D) and 3 weeks (E) deprogramming (CGRP downregulation), proliferation, and outgrowth into surrounding region of an mCherry-labeled NE clone has occurred to restore surrounding epithelium.

(F) Rare NEB with two clonal outgrowths (mCherry, mCerulean) 3 weeks after injury. Each clone occupies a separate territory; boxed region (F′) shows clonal boundary (arrowhead) without cell intermingling.

(G) Size of monoclonal outgrowths (Rainbow-labeled CGRP^{-} cells/clone). NEBs without outgrowths are indicated but not included in box-and-whisker plots and median calculations. Median values, 0, 0, 103, 237 cells; n, NEBs scored, 2–4 mice/time point; dotted line, detection limit.

(H) Clonal outgrowths per NEB 3 weeks after injury (n = 100 NEBs, 2 mice). Red, binomial fit. Bars, 50 μm (B–F), 10 μm (F′).

See also Figure S2.

type 2 (*Lyz2*; 2/8), or stromal cells (*Pdgfra*; 1/8) in a mutually exclusive pattern (Figures 4B and S3I). Thus, some isolated NE cells that express *Notch2* (Figures 4B and S3H) appear to activate Notch signaling (*Hes1* expression) and initiate NE deprogramming and reprogramming to other pulmonary fates, presumably in response to the extreme injury of mechanical/proteolytic tissue dissociation for scRNA-seq (van den Brink et al., 2017; Wu et al., 2017). Although there are other potential technical explanations for these transitional cells, studies below demonstrate a requirement for Notch signaling in NE reprogramming after airway injury *in vivo*.

Notch Signaling Initiates NE Deprogramming after Injury

We examined Notch pathway activation by airway injury (Figure 5A). Before injury, Hes1 was undetectable in NEBs (Figures 5B and 5D; Table S4), confirming the pathway is normally quiescent in NE cells (Ito et al., 2000). However, at 3 and 5 days after injury, rare nuclear Hes1-positive cells (0.5%–1%) were detected, increasing to 3% (1–3/NEB) at day 7 when NE deprogramming initiates (Figures 5C–5E; Table S4). This corresponded with the low efficiency of NE reprogramming, which typically involves just a single cell per NEB (Figure 3). Hes1-positive cells were usually (64%, 14 of 22 cases) located

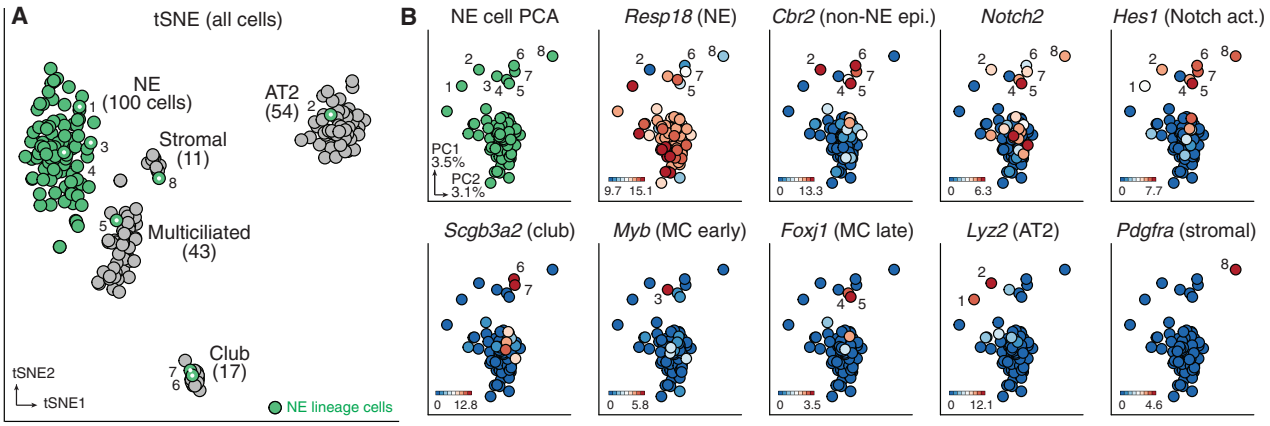

Figure 4. scRNA-Seq Reveals Notch Activation in NE Cells Undergoing Reprogramming

(A) Two-dimensional t-SNE projection of clustered scRNA-seq expression profiles of lineage-labeled NE cells (green circles, obtained using *Ascl1*^{CreER} [9 cells] or *CGRP*^{CreER} [91 cells]) and 125 other pulmonary cells (gray) from adult mice. Number of cells and identity (by canonical pulmonary markers) of each cluster is indicated. Cells 1–8 (central white dot) are NE cells with "transitional" expression profiles, some of which cluster with other cell types indicating active (or complete) lineage reprogramming.

(B) PCA of lineage-labeled NE cells in (A), with percent of total variance explained by PC1 and PC2 shown in first panel and rest showing cell expression levels of indicated genes (and cell type or pathway they mark). Transitional cells 1–8 are indicated. Most transitional cells (but few other NE cells) express *Notch2* and its target *Hes1* and are turning off NE marker *Resp18* and turning on non-NE pan-epithelial marker *Cbr2* and other cell type markers (bottom row; MC, multiciliated; AT2, alveolar type 2). Expression scales, $\log_2$ TPM+1 for ranges indicated.

See also Figure S3 and Table S3.

peripherally in the NEB (Figure 5C), suggesting that among the Notch ligands expressed in and around NEBs (Xu et al., 2010) (Figures S4A–S4M), the activating signal likely comes from injured epithelium rather than within the NEB itself. Thus, Notch pathway is activated at the right time, in an appropriate position, and to the expected extent to initiate NE cell deprogramming after injury.

Systemic delivery of the inhibitor dibenzazepine (DBZ) (Milano et al., 2004) during the deprogramming period (days 5–10 after injury) prevented Notch pathway activation (Figures S5A–S5C) and abrogated (84% reduction) NE deprogramming, amplification, and outgrowth (Figures 5G–5J). Conversely, mosaic expression of a constitutively active Notch fragment (N1ICD-IRES-nEGFP) (Murtaugh et al., 2003) in NE cells *in vivo* (Figure 5K) resulted in cell-autonomous induction of Hes1 and *Nrarp* (Figures S4O and S4U), and concurrent loss of CGRP expression (Figures 5L and 5M). This indicates Notch signaling can induce deprogramming even in the absence of injury. However, constitutively active Notch did not trigger expression of markers of other fates, including club (Scgb1a1) and variant club (*Upk3a*), multiciliated (Foxj1), and AT2 (Sftpc) (Figures S4N and S4R–S4U), or alter expression of proximal airway marker Sox2 or pan-epithelial E-cadherin (Figures S4P and S4Q). It also did not induce proliferation of deprogrammed cells (Figures S5I and S5J). We conclude Notch activation is necessary and sufficient for NE deprogramming, but amplification and reprogramming to other fates requires additional (or sustained) injury signals.

Rb and p53 Control Self-Renewal of NE Stem Cells

Although Notch controls deprogramming, the pathway was activated too late and in too few cells to mediate the early phase (week 1) of the injury response (Figure 5D). Indeed, Notch inhibition by DBZ on days 1–6 after injury did not alter self-renewal (Figures S5D–S5G) nor did Notch manipulations induce or alter NE dispersal (Figures S5I–S5N). Furthermore, the early and late phases are not contingently coupled: EdU labeling showed over half the nuclear Hes1-positive NE cells induced by injury (11 of 19, 58%) had not previously proliferated (Figure 5F; Table S4), none of the 8 transitional NE cells identified by scRNA-seq had a proliferative signature (Figure S5H), and constitutive Notch activation in NE cells did not induce ectopic proliferation (Figures S5I and S5J). We conclude Notch signaling specifically initiates deprogramming, and the early phase of the stem cell program must be controlled by another pathway and may need to terminate (e.g., NE^{stem} return to quiescence) before the second phase.

Given the established roles of Rb and p53 in cell-cycle regulation (Sherr, 1996) and their universal inactivation in SCLC (George et al., 2015), we investigated their function in regulating NE stem cell proliferation. We deleted conditional alleles of *Rb* (*Rb*^{f}) (Sage et al., 2003) and *p53* (*p53*^{f}) (Jonkers et al., 2001) from NE cells by tamoxifen induction of *Ascl1*^{CreERT2}, with *Rosa26*$^{LSL\text{-}ZsGreen}$ crossed in to label the mutant NE cells. We then measured cumulative NE proliferation with EdU for 1 week following injury and in mock-injured controls (Figure 6A). We found that, even in the absence of injury, 5% of Rb/p53-deficient NE cells (~1–2/NEB) proliferated during the week, whereas wild type controls remained quiescent (Figures 6B, 6C, and 6H). Thus, Rb/p53 prevent injury-independent proliferation of a small subpopulation of NE cells.

To determine if proliferating cells were the same NE subpopulation that proliferates after injury (NE^{stem}), we again used the dual nucleoside (EdU and BrdU) approach. This time though,

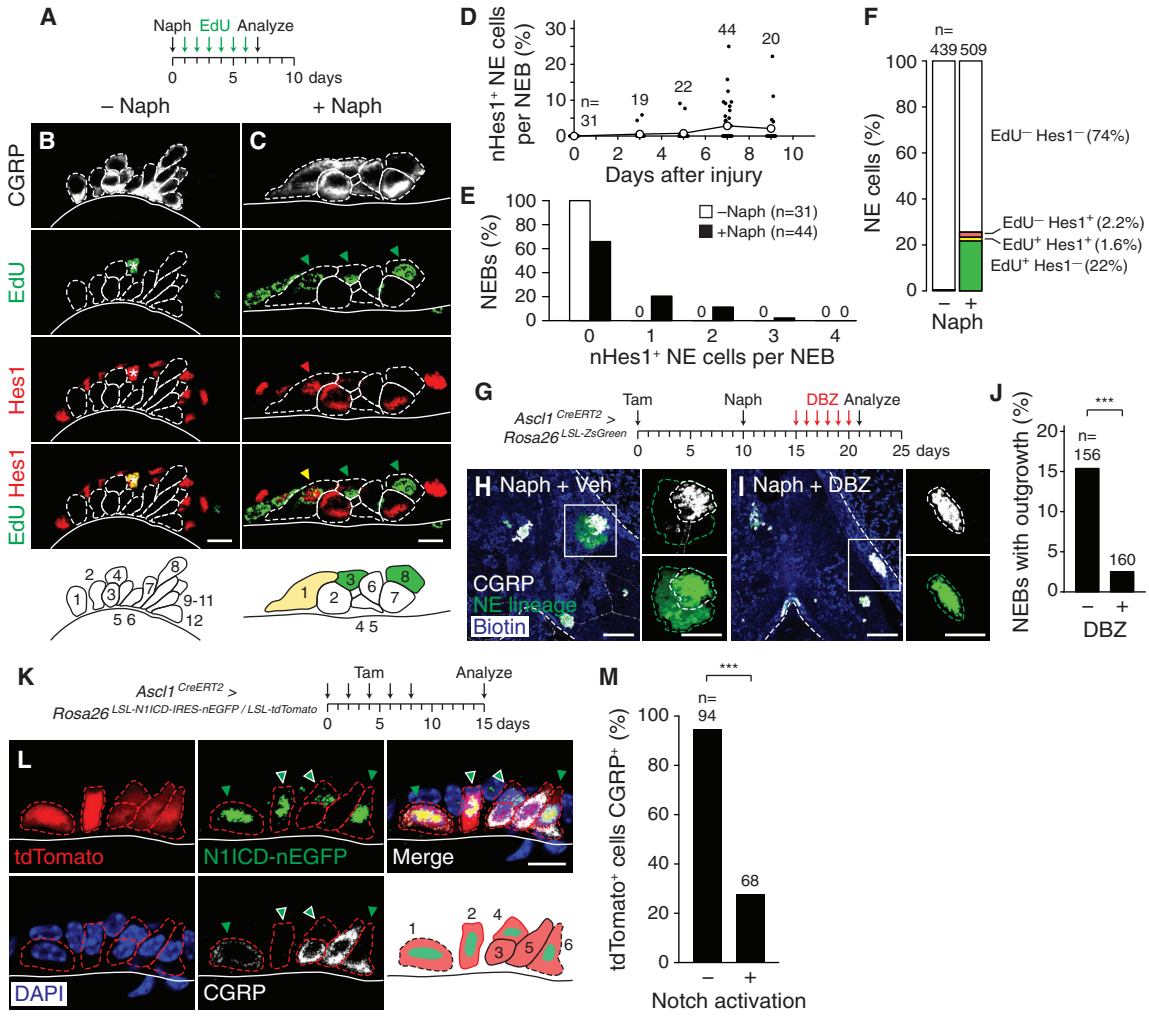

Figure 5. Notch Function in NE Reprogramming *In Vivo*

(A) Assessing NE proliferation and Notch pathway activation (Hes1 induction) after injury.

(B and C) Optical sections of NEBs from mock- (B, NEB103 Table S4) or naphthalene-injured mice (C, NEB140) 1 week after injury then stained (CGRP, Hes1) and click chemistry for EdU. Note single, peripheral NE cell (C, cell 1) that proliferated (EdU^+) and shows Notch activation (nuclear $Hes1^+$). Dashed outlines, individual NE cells (numbered in schematics); arrowheads, EdU^+ NE cells (green), $nHes1^+$ NE cell (red), EdU^+ $nHes1^+$ NE cell (yellow); asterisk, EdU^+ $nHes1^+$ non-NE cell.

(D) Time course of Notch activation ($nHes1^+$ NE cells) in NEBs. Mean values (open circles), 0, 0.5, 0.8, 2.8, 2.1%; n, NEBs scored, 2 mice/condition.

(E) Quantification of Notch-active NE cells at day 7 in (D). n, NEBs scored.

(F) Distribution of EdU^+, $nHes1^+$, double-positive, and double-negative $CGRP^+$ NE cells at day 7. n, NE cells scored, 17 (control), 30 (naph) NEBs in (D).

(G) Assessing Notch pathway requirement for NE deprogramming by Notch inhibitor DBZ injection during deprogramming. NE cells are lineage labeled by tamoxifen induction prior to injury.

(H and I) Bronchial branches (dashed outlines) from NE lineage-labeled (ZsGreen, "NE lineage"), naphthalene-injured mice treated with vehicle (H) or DBZ (I), stained for CGRP with biotin (epithelium) counterstain. Insets: boxed regions showing NEB (white dashed outlines) and outgrowth boundaries (green dashed outlines). Note no outgrowth in (I).

(J) Quantification of DBZ effect in (H) and (I). n, NEBs scored, 3 (vehicle), 4 (DBZ) mice; ***$p < 10^{-6}$, two-sided binomial test.

(K) Test of Notch sufficiency for deprogramming. Tamoxifen induces permanent expression of activated Notch (N1ICD) and nuclear marker (nEGFP, ~40% NE cells due to inefficient recombination) plus cytoplasmic lineage label (tdTomato, ~100% NE cells) in adult NE cells, which were later analyzed by CGRP stain and DAPI (nucleus) counterstain.

(L) NEB (cells outlined) 1 week after induction. Notch-activated cells ($nEGFP^+$, green dots in schematic) show low (green arrowheads; cells 1, 6) or no CGRP (white arrowheads with green fill; cells 2, 4), indicating NE deprogramming.

(M) Quantification of deprogramming (CGRP loss) in (L) with ($nEGFP^+$, 42% NE cells) or without ($nEGFP^-$, 58%) Notch pathway activation. n, NE cells scored, 10 NEBs, 4 mice; ***$p < 10^{-15}$, two-sided binomial test. Bars, 10 μm (B, C, and L), 100 μm (H and I).

See also Figures S4 and S5.

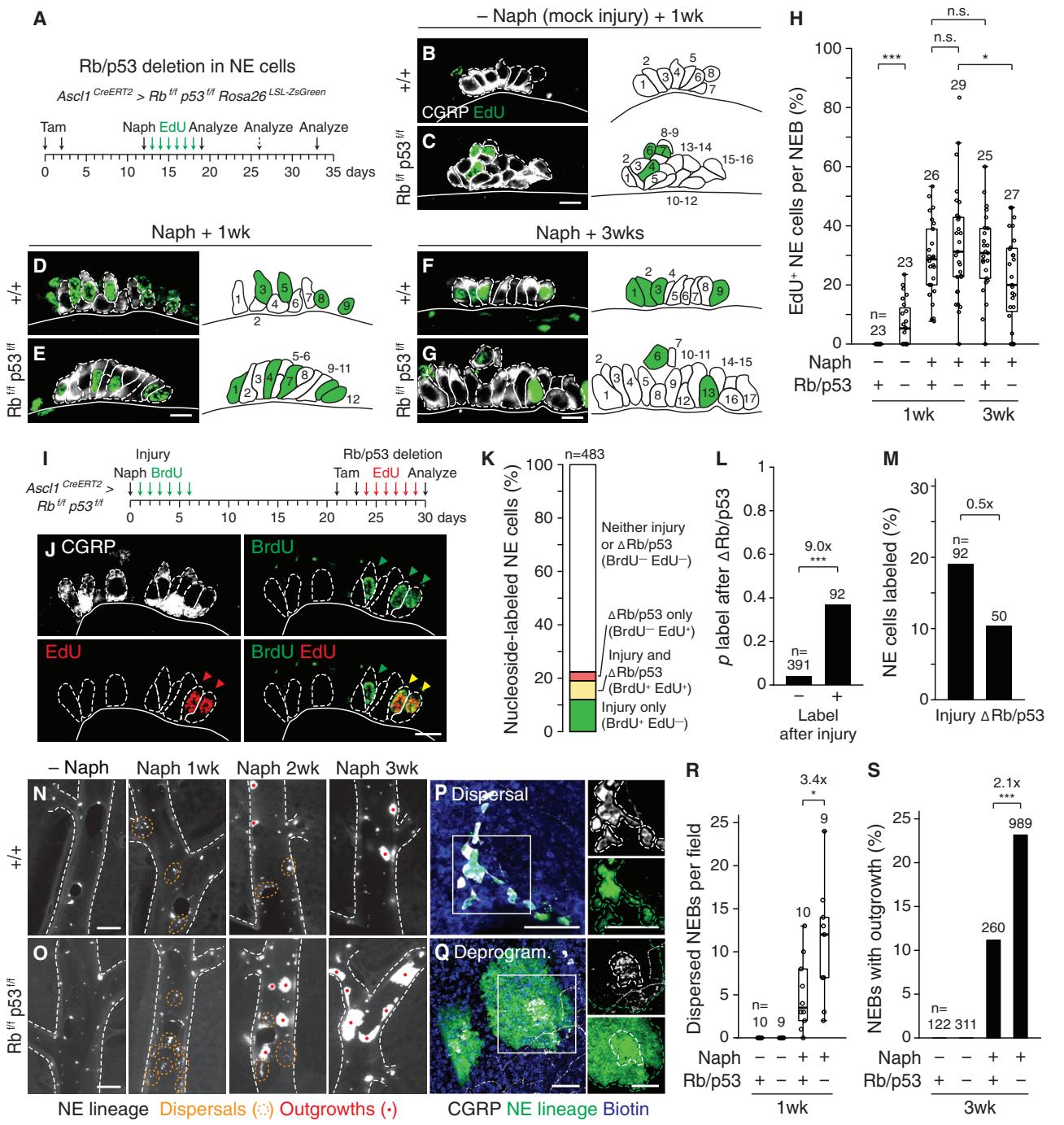

Figure 6. Effect of Rb and p53 on NE Stem Cell Function

(A) Lineage labeling and conditional deletion of *Rb* and *p53* in NE cells to assess role in NE stem cell proliferation (EdU incorporation, B–H), dispersal (N–P and R), and deprogramming/outgrowth (N, O, Q, and S).

(B–G) EdU incorporation in wild type ($^{+/+}$; B, D, and F) and Rb/p53-deficient ($Rb^{f/f}$ $p53^{f/f}$; C, E, and G) NEBs at indicated times (B–E, 1 week; F and G, 3 weeks) after mock (B and C) or naphthalene injury (D–G). Dashed outlines, NE cells. In Rb/p53 deletion, some NE cells proliferate without injury (C, cells 4,6,7).

(H) Quantification of (B)–(G). Wild-type values (Figure 1D) included for comparison. Median values, 0, 5, 29, 31, 31, 20%; n, NEBs scored, 2–4 mice/condition; ***$p < 10^{-3}$, *$p = 0.04$, two-sided Mann-Whitney U tests with Benjamini-Hochberg adjustment. Only the normal fraction of NE cells proliferated after injury in Rb/p53-deficient NEBs (D and E). EdU^+ NE cells in Rb/p53-deficient NEBs declined between 1 and 3 weeks after injury (G), indicating the cells continued proliferating and diluted the EdU label.

(I) Separate tracing of NE proliferation after airway injury (BrdU) and after tamoxifen-induced Rb/p53 deletion (EdU).

(legend continued on next page)

instead of the second round of injury, we deleted Rb/p53 using *Ascl1*^{CreERT2} (Figure 6I). We found that most NE cells (68%) that proliferated following Rb/p53 deletion (EdU-positive, 10% of total NE cells) had also proliferated after injury (BrdU/EdU double-positive) when the cells were wild type, despite their numerical minority (19% of total NE cells BrdU-positive) (Figures 6J, 6K, and 6M; Table S5). Indeed, there was a 9-fold bias for proliferation following Rb/p53 deletion if a NE cell had previously proliferated after injury (Figure 6L), similar to the 10-fold bias following a second round of injury (Figure 1L). Thus, most NE cells are refractory to Rb/p53 deletion, and the Rb/p53-sensitive cells are part of the same subpopulation as those activated by injury (i.e., NE^{stem} cells). Consistent with this, Rb/p53 deletion in conjunction with injury did not significantly increase the fraction of proliferating NE cells beyond that induced by injury alone (Figures 6D, 6E, and 6H).

Although Rb/p53 deletion and injury both induce NE^{stem} proliferation, there was an important difference. Whereas proliferating wild-type NE^{stem} cells returned to quiescence 1 week after injury, as shown by retention of the EdU label over the following 2 weeks (29% EdU-positive cells after 1 week of EdU labeling after injury, versus 31% after 2 additional weeks without EdU; $p = 0.4$, Mann-Whitney U test) (Figures 6F and 6H), Rb/p53-deficient NE^{stem} cells exhibited a 36% decrease in EdU labeling over the same period (31% after 1 week versus 20% after 2 additional weeks; $p = 0.04$, Mann-Whitney U test) (Figures 6G and 6H). This indicates Rb/p53-deficient NE^{stem} cells failed to reestablish quiescence. Indeed, Rb/p53-deficient NEBs increased in size by 15% during the 2-week interim, while wild-type controls were unchanged (Figures S6A–S6C). Thus, in addition to preventing proliferation of NE^{stem} in the absence of injury, Rb/p53 are required for timely reestablishment of quiescence after injury.

There were two other effects of Rb/p53 deletion on NE behavior after injury: 3.4-fold more Rb/p53-deficient NEBs showed cell dispersals (Figures 6N–6P and 6R) and 2.1-fold more showed clonal outgrowths (Figures 6N, 6O, 6Q, and 6S), increasing NEB contribution to repair of the bronchial surface from 4% in wild type to 22% after Rb/p53 deletion (Figures S2D–S2F). However, neither dispersal nor clonal outgrowth occurred in Rb/p53-deficient NEBs without injury (Figure 6O, 6R, 6S). Finally, although these injury-induced behaviors were more frequent in Rb/p53-deficient NEBs, the cell behaviors themselves were unchanged: NE cell dispersal showed the usual timing, migratory morphology, number of satellites around each NEB, and distance traveled from the NEB after injury (Figures 6N–6P and S6D–S6G), and outgrowths showed their normal timing and pattern (Figures 6N, 6O, and 6Q) with predominantly monoclonal outgrowths that maintained clonal boundaries (Figures S6H and S6I). Thus, in addition to preventing injury-independent NE^{stem} proliferation, Rb/p53 desensitize NEBs to injury-induced dispersal and reprogramming signals.

Notch2 Is a Marker of NE^{stem}

PCA of transcriptomic profiles of 260 lineage-labeled NE cells (Figures 4B and S3J) did not uncover a discrete NE subpopulation consistent with the stem cell pool size (17%, Figure 1G). This implies NE^{stem} have a similar expression profile as "bulk" NE cells, perhaps only differing in expression of a small number of genes that confer stem cell function. One candidate was *Notch2*, because Notch signaling plays an important role in the stem cell program (Figure 5), and *Notch2* expression was detected by scRNA-seq in 16% of NE cells and enriched 5-fold in transitional cells (Figures 4B and S3H). Single-molecule fluorescence *in situ* hybridization (smFISH; RNAscope) detected *Notch2* in a similar fraction of NE cells (18%, 1–9/NEB) scattered in the NEB like NE^{stem} (Figures 7A and S7A–S7C).

To determine if *Notch2* marks NE^{stem}, we probed its expression in cells that proliferate after injury (Figure 7B). We found 40% of EdU-positive NE cells were also *Notch2*-positive, a 2.2-fold enrichment over *Notch2*-negative cells (Figures 7C–7E). This suggested *Notch2* is an enriched but imperfect marker of NE^{stem}, or a faithful marker that labels only NE^{stem} but not its other daughter cells (both of which are labeled by EdU). Consistent with the latter, the fraction of *Notch2*-expressing NE cells was not increased 1 week after naphthalene injury (23% versus 24% after mock injury) (Figure 7D), when NE^{stem} have undergone 1–2 rounds of proliferation (Figures 1A–1H and S1A–S1L), and most EdU-positive *Notch2*-negative NE cells detected after injury (78%) were apposed to an EdU-positive *Notch2*-positive

(J) Optical section of NEB (NEB157 Table S5) sequentially treated as above then analyzed for CGRP, BrdU, and EdU. Dashed outlines, NE cells; arrowheads, BrdU$^+$ (green), EdU$^+$ (red), and EdU$^+$ BrdU$^+$ NE cells (yellow). Both NE cells that proliferated after Rb/p53 deletion (EdU$^+$) also proliferated after injury while still wild type (BrdU$^+$).

(K) Quantification of (J) showing distribution of CGRP$^+$ NE cells that proliferated in both rounds, only after injury, or only after Rb/p53 deletion. n, NE cells scored, 18 NEBs, 3 mice.

(L) Derived probability (p) of NE cell proliferating after Rb/p53 deletion stratified by whether it proliferated after injury. n, NE cells scored; ***$p < 10^{-15}$, hypergeometric test of BrdU/EdU overlap in (K).

(M) Fraction of NE cells that proliferated after injury and after Rb/p53 deletion. Decreased labeling after Rb/p53 deletion is consistent with its less efficient induction of proliferation compared to injury. n, NE cells scored.

(N and O) Wild type (N) and Rb/p53-deficient NEBs (O) as in (A) but with lineage-labeled NE cells ("NE lineage") visualized in bronchial branches (white outlines) at indicated times after mock or naphthalene injury. Note increased fragmenting/dispersal (orange outlines) of Rb/p53-deficient NEBs 1 week after injury, and increased deprogramming to form large outgrowths (red dots) at 2 and 3 weeks.

(P and Q) Close-ups of Rb/p53-deficient NEBs as in (O) showing CGRP, NE lineage label (ZsGreen), and epithelium (biotin) to better visualize dispersal (P, 1 week after injury) and deprogramming (Q, 3 weeks after injury). Insets: split channels of boxed regions (white outlines, NEB boundaries and satellite cells; green outlines, outgrowth boundaries).

(R and S) Quantification of dispersal one week after injury (R; n, fields scored, 3–5 mice/condition; *$p = 0.05$, two-sided Mann-Whitney U test) and deprogramming/outgrowth at three weeks (S; n, NEBs scored, 4 mice/condition; ***$p < 10^{-25}$, two-sided binomial test). Bars, 10 μm (B–G and J), 100 μm (P and Q), and 500 μm (N and O).

See also Figures S2 and S6.

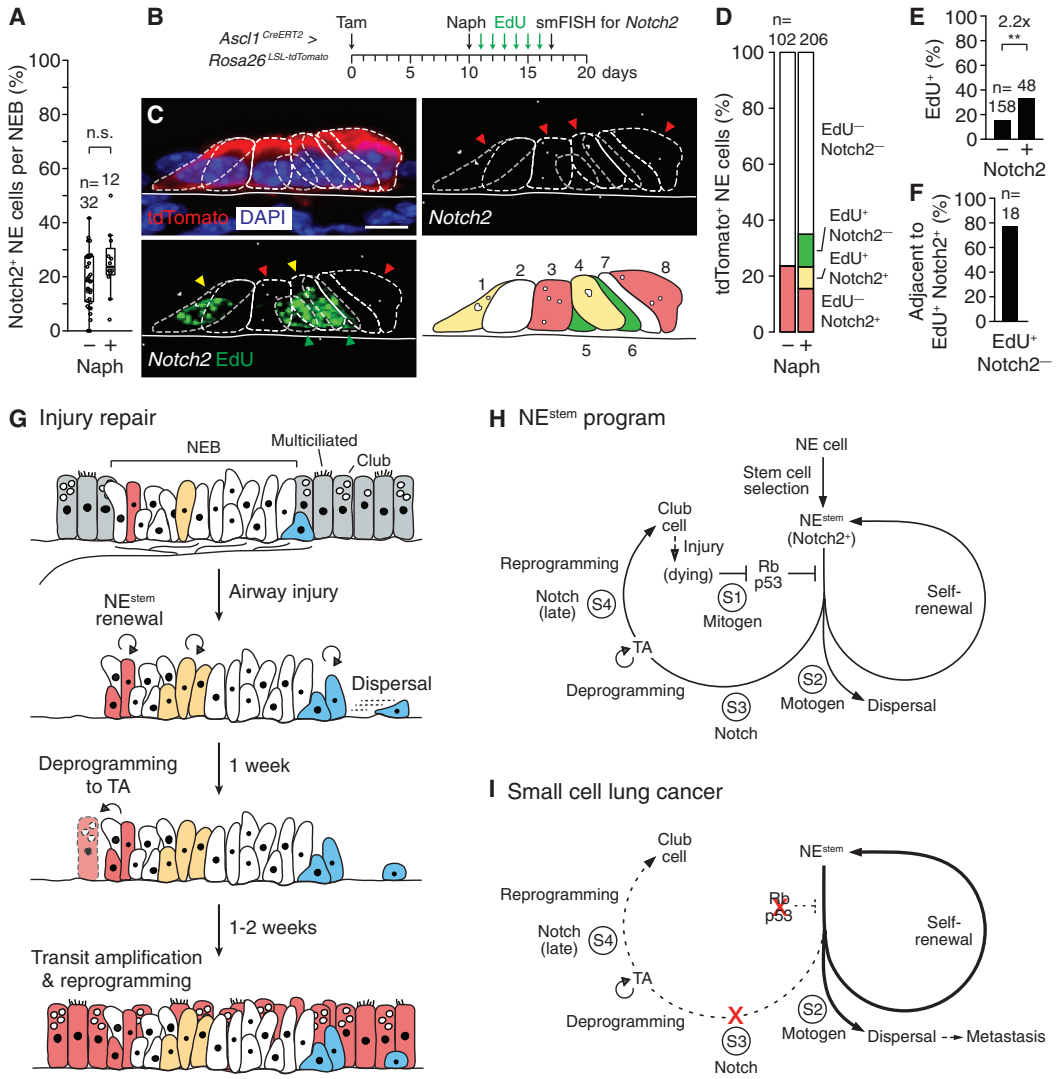

Figure 7. NE^{stem} Marker and Role in Lung Repair and Cancer

(A) *Notch2* mRNA expression (smFISH) before and 1 week after naphthalene injury (see representative image in Figure S7B). Median values, 18, 24%; n, NEBs scored, 2 mice/condition.

(B) Assessing NE^{stem} activity (proliferation) of *Notch2*-expressing NE cells after injury.

(C) Injured NEB (white, NE cell outlines) showing smFISH for *Notch2* (white puncta), click chemistry for EdU, tdTomato stain, and DAPI. Two of four *Notch2*$^+$ NE cells (yellow and red arrowheads, cells 1, 3, 4, and 8 in schematic with *Notch2* puncta in white) proliferated (EdU$^+$, cells 1 and 4). Two other EdU$^+$ NE cells (green arrowheads, cells 5 and 6) are *Notch2*$^-$ but adjacent to an EdU$^+$ *Notch2*$^+$ NE cell (cell 4) they may have arisen from. Bar, 10 μm.

(D) Quantification of (C). n, NE cells scored, 6 (control), 12 (naph) NEBs (subset of NEBs in A).

(E) Fraction of NE cells that proliferated (EdU$^+$) after injury, stratified by *Notch2* expression. n, NE cells scored (from D); **$p < 10^{-2}$, hypergeometric test of EdU/*Notch2* overlap in (D).

(F) Fraction of EdU$^+$ *Notch2*$^-$ cells adjacent to EdU$^+$ *Notch2*$^+$ cells in NEBs, suggesting shared clonal origin. n, NE cells scored (from D, scored NEBs had ≥1 EdU$^+$ *Notch2*$^+$ cell).

(G) NE^{stem} function in repair. Each innervated NEB (white cells) harbors several NE^{stem} cells (red, yellow, cyan) that are fully differentiated but quiescent. Upon injury of neighboring cells (gray) each NE^{stem} self-renews and some disperse into injured area (cyan cell). Almost all reestablish quiescence by 1 week except a rare cell that deprograms to a transit amplifying (TA) state (red cell) and proliferates for 1–2 weeks and reprograms to mature bronchial fates, forming monoclonal patch of regenerated epithelium around NEB.

(H) NE^{stem} regulation. *Notch2*$^+$ NE^{stem} senses three injury signals (S1–S3). One is mitogen (S1) from dying cells that inactivates Rb and p53, derepressing NE^{stem} self-renewal. S2 is motogen that induces dispersal. S3 is Notch ligand that initiates deprogramming to TA state. S4 is Notch ligand active late in repair that induces reprogramming to mature bronchial fates.

(I) SCLC initiation. Loss of Rb and p53 in NE^{stem} triggers constitutive self-renewal (independent of S1), and sensitizes NE^{stem} to S2 and S3 so even low-grade injury (e.g., cigarette smoke) provides enough S2 for dispersal and early metastasis. Notch receptor loss prevents deprogramming and reprogramming by S3 and S4 to less malignant cell fate, locking in self-renewal (tumor growth) and dispersal (metastasis).

See also Figure S7.

NE cell in the same NEB (Figure 7F) and thus likely daughters of the neighboring *Notch2*-positive NE^{stem} parent. This supports a model in which *Notch2* marks NE^{stem}, and its expression is asymmetrically inherited (or downregulated) in daughter cells.

DISCUSSION

NEBs harbor a minor subpopulation of NE cells, typically 2–4 per NEB, with reserve stem cell activity (Figure 7G). These NE^{stem} appear to be fully differentiated and presumably functional in sensing and signaling during homeostasis like bulk NE cells (Cutz et al., 2013; Garg et al., 2019) (Figure S7D), but following severe airway injury display features of classical stem cells (Morrison and Spradling, 2008; Potten and Loeffler, 1990). They proliferate in the NEB niche to generate additional NE cells (self-renew), and some disperse from the niche forming satellite cells. Self-renewal and dispersal subside in the week after injury, around the time rare cells, typically limited to one per NEB, downregulate NE markers (deprogram) and continue proliferating. Over the next 2 weeks, daughters of these transit amplifying (TA) cells grow out from the niche, forming a large, coherent, monoclonal patch of newborn epithelial cells surrounding the NEB, reprogramming to club, multiciliated, and perhaps other fates to regenerate the lost epithelium.

The results begin to define the molecular pathways that select and control the stem cells (Figure 7H). *Notch2* marks them, and Rb/p53 maintain their quiescence. Compound deletion of Rb/p53 induces slow but persistent NE^{stem} renewal, even in the absence of injury. The switch to TA is controlled by Notch: injury activates the pathway at the appropriate time and in the small number of switching NE cells, and blocking Notch signaling pharmacologically or by *Rbpj* or *Pofut1* deletion (Yao et al., 2018) prevents the switch, whereas a constitutively active Notch deprograms NE identity even in the absence of injury. This Notch signal does not induce full reprogramming to other fates, which occurs days or weeks after deprogramming (Yao et al., 2018) and presumably requires a second Notch signal (Xing et al., 2012).

Multiple Injury-Induced Signals Control NE^{stem}

Our data provide evidence for at least three injury-induced signals that control NE^{stem} (Figure 7H). One is a mitogen (S1) that inhibits Rb and/or p53, releasing the block on stem cell renewal. This must be an early and diffuse signal with access throughout the NEB because most NE^{stem} respond to injury. The signal must also be transient to allow restoration of Rb/p53 function and reestablish stem cell quiescence once enough cells have been generated. The second signal (S2) is a motogen that promotes dispersal. This could be reactivation of the slithering signal(s) that drives migration of NE progenitors into clusters during development (Kuo and Krasnow, 2015; Noguchi et al., 2015) or loss of an attractive signal (e.g., Slit) that maintains clusters once formed (Branchfield et al., 2016). The third (S3) is the Notch signal noted above that triggers NE^{stem} switch to TA. Unlike the first two signals, this deprogramming signal comes late, about a week after injury, and is highly localized, typically activating Notch pathway and the switch in no more than a single peripheral NEB cell. Finally, Notch signaling is likely reactivated days or weeks later (S4) when TA cells acquire mature club and multiciliated fates to complete restoration of the epithelium.

A future goal is to molecularly identify these signals and their sources and elucidate how they are induced by injury and how they interact. For example, multiple Notch ligands are expressed in and around the NEB, before and after injury. How they interact with each other and with the mitogen might explain the delay in Notch signaling and deprogramming until a week after injury, when proliferation subsides. A related goal is to identify the full set of genes that mark NE^{stem} and confer sensitivity to the signals and other stem cell properties. Our results identify *Notch2* as one marker, and suggest its expression is asymmetrically inherited through each division to maintain a fixed pool of stem cells. There must be additional genes that endow NE^{stem} with receptivity to the other signals, but there cannot be many such genes because NE^{stem} did not form a distinct cluster by scRNA-seq.

NE^{stem} and SCLC

The results support NE^{stem} as tumor-initiating cells for SCLC (Figure 7I). SCLC has long been speculated to arise from pulmonary NE cells because of morphological and molecular similarity (Bensch et al., 1968; Nicholson et al., 2002), and because deletion of obligate SCLC tumor suppressors *Rb* and *p53* in mouse pulmonary NE cells gives rise months later to similar tumors (Park et al., 2011a; Song et al., 2012; Sutherland et al., 2011). However, only rare NE cells are transformed in the mouse model (Park et al., 2011a, 2011b). Our studies show these are NE^{stem}, which begin proliferating slowly and continuously right after Rb/p53 deletion. Thus, we propose that NE^{stem} are the primary cell of origin of SCLC (although rare tumors may have other origins; Huang et al., 2018; Yang et al., 2018), and tumor initiation results from almost immediate and persistent activation of NE^{stem} renewal following loss of *Rb* and *p53*.

Rb/p53 also desensitize NE^{stem} to the dispersal and deprogramming signals. Hence, if injury occurs after loss of Rb/p53, more NE cells will disperse and deprogram. Dispersal may explain the early metastatic spread of SCLC, an unfortunate hallmark of the disease (Semenova et al., 2015). Increased sensitivity to deprogramming signal would shunt NE cells into less malignant (or less Rb/p53-sensitive) cell fates, which would be tumor suppressive. This would explain the frequent (25%) occurrence of Notch receptor loss-of-function mutations in human SCLCs (George et al., 2015), which would prevent deprogramming and lock in NE^{stem} identity of the tumors (Figure 7I). Indeed, Notch activation can initiate reprogramming in SCLC cells (Lim et al., 2017), implying Notch functions similarly in NE^{stem} and SCLC. The mouse model can be used to study the earliest oncogenic events and uncover new approaches for early detection and elimination of tumors before they turn deadly.

Differentiated Stem Cells and Cancer

NE^{stem} show striking parallels to AT2 stem cells ($AT2^{stem}$) that maintain the lung's gas exchange surface (Logan and Desai, 2015). Unlike prototypical stem cells, generally viewed as immature cells with dedicated ("professional") stem cell function

(Morrison and Spradling, 2008; Potten and Loeffler, 1990), both types of lung stem cells are rare subpopulations of differentiated cell types with physiological functions separate from their stem cell function. Stem cell activity is low ($AT2^{stem}$) or undetectable (NE^{stem}) until injury, and genetic alterations in the stem cells initiate deadly lung cancers (NE^{stem}, SCLC; $AT2^{stem}$, adenocarcinoma) by constitutively activating stem cell renewal and crippling the ability to reprogram to less tumorigenic fates (Desai et al., 2014; Nabhan et al., 2018; Tammela et al., 2017). Despite parallels, these two types of stem cells have disparate morphologies and functions, and little in common in the cell types they spawn or their regulatory programs, including the signals that control them, oncogenes that transform them, and therapies that target their transformed progeny.

A growing number of differentiated cell types have been found to harbor subpopulations with stem cell activity, including other lung cell types (Leach and Morrisey, 2018; Liu et al., 2019; Salwig et al., 2019; Sheikh et al., 2015) and a variety in other organs (Clevers and Watt, 2018; Merrell and Stanger, 2016). Examples in insects have even emerged (Weaver and Krasnow, 2008). Differentiated stem cells, each with little morphological and few molecular differences from its non-stem counterparts, could turn out to be the most common type of adult stem cell and source of cancer.

STAR★METHODS

Detailed methods are provided in the online version of this paper and include the following:

- KEY RESOURCES TABLE
- LEAD CONTACT AND MATERIALS AVAILABILITY
- EXPERIMENTAL MODEL AND SUBJECT DETAILS
  - Animals
- METHOD DETAILS
  - Tamoxifen induction of Cre recombination
  - Airway injury with naphthalene
  - Cell proliferation analysis by EdU and BrdU labeling
  - Pharmacological inhibition of Notch signaling with dibenzazepine (DBZ)
  - Immunohistochemistry
  - Single molecule fluorescence *in situ* hybridization (smFISH)
  - Microscopy and imaging
  - Simulations of NE proliferation after injury
  - NE cell purification by Fluorescence-Activated Cell Sorting (FACS)
  - Microfluidic single cell capture and cDNA library preparation
  - Single cell mRNA sequencing
  - Single cell mRNA sequencing analysis
  - Analysis of additional mouse NE cell scRNA-seq profiles
- QUANTIFICATION AND STATISTICAL ANALYSIS
  - Quantification of NEB size, outgrowths, and cell dispersals
  - Statistical analysis
- DATA AND CODE AVAILABILITY

SUPPLEMENTAL INFORMATION

Supplemental Information can be found online at https://doi.org/10.1016/j.cell.2019.09.010.

ACKNOWLEDGMENTS

For advice and assistance, we thank Maya Kumar (microscopy); Cathy Crumpton, Bianca Gomez, and Stanford FACS Facility (flow sorting); Spyros Darmanis, Neo Chung, Dominic Grün, Gary Mantalas, Norma Neff, Ben Passarelli, Sopheak Sim, Barbara Treutlein, Angela Wu, and Brian Yu (scRNA-seq); Pao-Tien Chuang, Tushar Desai, Jane Johnson, Julien Sage, and Irv Weissman (mouse lines); Jing Lim and Dian Yang (reagents, discussions); Tushar Desai, Maya Kumar, Ross Metzger, Lucy O'Brien, Julien Sage, Thomas Vierbuchen, and Kevin Yackle (comments on manuscript); and members of our lab (experiments, interpretations, comments on manuscript). This work was supported by NHLBI (U01-HL099995), NCI (U01-CA23185), HHMI, Virginia and D.K. Ludwig Fund for Cancer Research, an NSF Graduate Research Fellowship (Y.O.), Stanford Graduate Fellowship in Science and Engineering (Y.O.), and the Stanford Cancer Biology Program (NCI CA09302 to Y.O.). M.A.K. is an HHMI investigator.

AUTHOR CONTRIBUTIONS

Conceptualization, Y.O. and M.A.K.; Methodology, Y.O., E.R.R., D.P.R., S.C., and M.A.K.; Formal Analysis, Y.O., E.R.R., D.P.R., and S.C.; Investigation, Y.O.; Resources, C.S.K.; Writing – Original Draft, Y.O. and M.A.K.; Writing – Review & Editing, all authors; Supervision, M.A.K.; Funding Acquisition, Y.O., C.S.K., and M.A.K.

DECLARATION OF INTERESTS

The authors declare no competing interests.

Received: July 26, 2018
Revised: April 29, 2019
Accepted: September 5, 2019
Published: October 3, 2019

REFERENCES

Adriaensen, D., and Scheuermann, D.W. (1993). Neuroendocrine cells and nerves of the lung. Anat. Rec. *236*, 70–86.

Artavanis-Tsakonas, S., Rand, M.D., and Lake, R.J. (1999). Notch signaling: cell fate control and signal integration in development. Science *284*, 770–776.

Bensch, K.G., Corrin, B., Pariente, R., and Spencer, H. (1968). Oat-cell carcinoma of the lung. Its origin and relationship to bronchial carcinoid. Cancer *22*, 1163–1172.

Boers, J.E., den Brok, J.L., Koudstaal, J., Arends, J.W., and Thunnissen, F.B. (1996). Number and proliferation of neuroendocrine cells in normal human airway epithelium. Am. J. Respir. Crit. Care Med. *154*, 758–763.

Branchfield, K., Nantie, L., Verheyden, J.M., Sui, P., Wienhold, M.D., and Sun, X. (2016). Pulmonary neuroendocrine cells function as airway sensors to control lung immune response. Science *351*, 707–710.

Bray, N.L., Pimentel, H., Melsted, P., and Pachter, L. (2016). Near-optimal probabilistic RNA-seq quantification. Nat. Biotechnol. *34*, 525–527.

Chung, N.C., and Storey, J.D. (2015). Statistical significance of variables driving systematic variation in high-dimensional data. Bioinformatics *31*, 545–554.

Clausen, B.E., Burkhardt, C., Reith, W., Renkawitz, R., and Förster, I. (1999). Conditional gene targeting in macrophages and granulocytes using LysMcre mice. Transgenic Res. *8*, 265–277.

Clevers, H., and Watt, F.M. (2018). Defining adult stem cells by function, not by phenotype. Annu. Rev. Biochem. *87*, 1015–1027.

Cutz, E., Pan, J., Yeger, H., Domnik, N.J., and Fisher, J.T. (2013). Recent advances and contraversies on the role of pulmonary neuroepithelial bodies as airway sensors. Semin. Cell Dev. Biol. *24*, 40–50.

Desai, T.J., Brownfield, D.G., and Krasnow, M.A. (2014). Alveolar progenitor and stem cells in lung development, renewal and cancer. Nature *507*, 190–194.

Dobin, A., Davis, C.A., Schlesinger, F., Drenkow, J., Zaleski, C., Jha, S., Batut, P., Chaisson, M., and Gingeras, T.R. (2013). STAR: ultrafast universal RNA-seq aligner. Bioinformatics *29*, 15–21.

Garg, A., Sui, P., Verheyden, J.M., Young, L.R., and Sun, X. (2019). Consider the lung as a sensory organ: A tip from pulmonary neuroendocrine cells. Curr. Top. Dev. Biol. *132*, 67–89.

George, J., Lim, J.S., Jang, S.J., Cun, Y., Ozretić, L., Kong, G., Leenders, F., Lu, X., Fernández-Cuesta, L., Bosco, G., et al. (2015). Comprehensive genomic profiles of small cell lung cancer. Nature *524*, 47–53.

Grün, D., and van Oudenaarden, A. (2015). Design and analysis of single-cell sequencing experiments. Cell *163*, 799–810.

Grün, D., Muraro, M.J., Boisset, J.-C., Wiebrands, K., Lyubimova, A., Dharmadhikari, G., van den Born, M., van Es, J., Jansen, E., Clevers, H., et al. (2016). De novo prediction of stem cell identity using single-cell transcriptome data. Cell Stem Cell *19*, 266–277.

Guha, A., Vasconcelos, M., Zhao, R., Gower, A.C., Rajagopal, J., and Cardoso, W.V. (2014). Analysis of Notch signaling-dependent gene expression in developing airways reveals diversity of Clara cells. PLoS ONE *9*, e88848.

Hogan, B.L.M., Barkauskas, C.E., Chapman, H.A., Epstein, J.A., Jain, R., Hsia, C.C.W., Niklason, L., Calle, E., Le, A., Randell, S.H., et al. (2014). Repair and regeneration of the respiratory system: complexity, plasticity, and mechanisms of lung stem cell function. Cell Stem Cell *15*, 123–138.

Huang, Y.-H., Klingbeil, O., He, X.-Y., Wu, X.S., Arun, G., Lu, B., Somerville, T.D.D., Milazzo, J.P., Wilkinson, J.E., Demerdash, O.E., et al. (2018). POU2F3 is a master regulator of a tuft cell-like variant of small cell lung cancer. Genes Dev. *32*, 915–928.

Ito, T., Udaka, N., Yazawa, T., Okudela, K., Hayashi, H., Sudo, T., Guillemot, F., Kageyama, R., and Kitamura, H. (2000). Basic helix-loop-helix transcription factors regulate the neuroendocrine differentiation of fetal mouse pulmonary epithelium. Development *127*, 3913–3921.

Jarriault, S., Brou, C., Logeat, F., Schroeter, E.H., Kopan, R., and Israel, A. (1995). Signalling downstream of activated mammalian Notch. Nature *377*, 355–358.

Jiang, L., Schlesinger, F., Davis, C.A., Zhang, Y., Li, R., Salit, M., Gingeras, T.R., and Oliver, B. (2011). Synthetic spike-in standards for RNA-seq experiments. Genome Res. *21*, 1543–1551.

Jonkers, J., Meuwissen, R., van der Gulden, H., Peterse, H., van der Valk, M., and Berns, A. (2001). Synergistic tumor suppressor activity of BRCA2 and p53 in a conditional mouse model for breast cancer. Nat. Genet. *29*, 418–425.

Kim, E.J., Ables, J.L., Dickel, L.K., Eisch, A.J., and Johnson, J.E. (2011). Ascl1 (Mash1) defines cells with long-term neurogenic potential in subgranular and subventricular zones in adult mouse brain. PLoS ONE *6*, e18472.

Kuhn, C. (1988). Biotin stores in rodent lungs: localization to Clara and type II alveolar cells. Exp. Lung Res. *14*, 527–536.

Kuo, C.S., and Krasnow, M.A. (2015). Formation of a neurosensory organ by epithelial cell slithering. Cell *163*, 394–405.

Lafkas, D., Shelton, A., Chiu, C., de Leon Boenig, G., Chen, Y., Stawicki, S.S., Siltanen, C., Reichelt, M., Zhou, M., Wu, X., et al. (2015). Therapeutic antibodies reveal Notch control of transdifferentiation in the adult lung. Nature *528*, 127–131.

Leach, J.P., and Morrisey, E.E. (2018). Repairing the lungs one breath at a time: How dedicated or facultative are you? Genes Dev. *32*, 1461–1471.

Lim, J.S., Ibaseta, A., Fischer, M.M., Cancilla, B., O'Young, G., Cristea, S., Luca, V.C., Yang, D., Jahchan, N.S., Hamard, C., et al. (2017). Intratumoural heterogeneity generated by Notch signalling promotes small-cell lung cancer. Nature *545*, 360–364.

Liu, Q., Liu, K., Cui, G., Huang, X., Yao, S., Guo, W., Qin, Z., Li, Y., Yang, R., Pu, W., et al. (2019). Lung regeneration by multipotent stem cells residing at the bronchioalveolar-duct junction. Nat. Genet. *51*, 728–738.

Logan, C.Y., and Desai, T.J. (2015). Keeping it together: Pulmonary alveoli are maintained by a hierarchy of cellular programs. BioEssays *37*, 1028–1037.

Madisen, L., Zwingman, T.A., Sunkin, S.M., Oh, S.W., Zariwala, H.A., Gu, H., Ng, L.L., Palmiter, R.D., Hawrylycz, M.J., Jones, A.R., et al. (2010). A robust and high-throughput Cre reporting and characterization system for the whole mouse brain. Nat. Neurosci. *13*, 133–140.

Merrell, A.J., and Stanger, B.Z. (2016). Adult cell plasticity in vivo: de-differentiation and transdifferentiation are back in style. Nat. Rev. Mol. Cell Biol. *17*, 413–425.

Milano, J., McKay, J., Dagenais, C., Foster-Brown, L., Pognan, F., Gadient, R., Jacobs, R.T., Zacco, A., Greenberg, B., and Ciaccio, P.J. (2004). Modulation of notch processing by gamma-secretase inhibitors causes intestinal goblet cell metaplasia and induction of genes known to specify gut secretory lineage differentiation. Toxicol. Sci. *82*, 341–358.

Morrison, S.J., and Spradling, A.C. (2008). Stem cells and niches: mechanisms that promote stem cell maintenance throughout life. Cell *132*, 598–611.

Murtaugh, L.C., Stanger, B.Z., Kwan, K.M., and Melton, D.A. (2003). Notch signaling controls multiple steps of pancreatic differentiation. Proc. Natl. Acad. Sci. USA *100*, 14920–14925.

Nabhan, A.N., Brownfield, D.G., Harbury, P.B., Krasnow, M.A., and Desai, T.J. (2018). Single-cell Wnt signaling niches maintain stemness of alveolar type 2 cells. Science *359*, 1118–1123.

Nicholson, S.A., Beasley, M.B., Brambilla, E., Hasleton, P.S., Colby, T.V., Sheppard, M.N., Falk, R., and Travis, W.D. (2002). Small cell lung carcinoma (SCLC): a clinicopathologic study of 100 cases with surgical specimens. Am. J. Surg. Pathol. *26*, 1184–1197.

Noguchi, M., Sumiyama, K., and Morimoto, M. (2015). Directed migration of pulmonary neuroendocrine cells toward airway branches organizes the stereotypic location of neuroepithelial bodies. Cell Rep. *13*, 2679–2686.

O'Brien, K.A., Suverkropp, C., Kanekal, S., Plopper, C.G., and Buckpitt, A.R. (1989). Tolerance to multiple doses of the pulmonary toxicant, naphthalene. Toxicol. Appl. Pharmacol. *99*, 487–500.

Ooi, C.C., Mantalas, G.L., Koh, W., Neff, N.F., Fuchigami, T., Wong, D.J., Wilson, R.J., Park, S.-M., Gambhir, S.S., Quake, S.R., and Wang, S.X. (2017). High-throughput full-length single-cell mRNA-seq of rare cells. PLoS ONE *12*, e0188510.

Pardo-Saganta, A., Tata, P.R., Law, B.M., Saez, B., Chow, R.D.-W., Prabhu, M., Gridley, T., and Rajagopal, J. (2015). Parent stem cells can serve as niches for their daughter cells. Nature *523*, 597–601.

Park, K.-S., Liang, M.-C., Raiser, D.M., Zamponi, R., Roach, R.R., Curtis, S.J., Walton, Z., Schaffer, B.E., Roake, C.M., Zmoos, A.-F., et al. (2011a). Characterization of the cell of origin for small cell lung cancer. Cell Cycle *10*, 2806–2815.

Park, K.-S., Martelotto, L.G., Peifer, M., Sos, M.L., Karnezis, A.N., Mahjoub, M.R., Bernard, K., Conklin, J.F., Szczepny, A., Yuan, J., et al. (2011b). A crucial requirement for Hedgehog signaling in small cell lung cancer. Nat. Med. *17*, 1504–1508.

Peake, J.L., Reynolds, S.D., Stripp, B.R., Stephens, K.E., and Pinkerton, K.E. (2000). Alteration of pulmonary neuroendocrine cells during epithelial repair of naphthalene-induced airway injury. Am. J. Pathol. *156*, 279–286.

Picelli, S., Björklund, A.K., Faridani, O.R., Sagasser, S., Winberg, G., and Sandberg, R. (2013). Smart-seq2 for sensitive full-length transcriptome profiling in single cells. Nat. Methods *10*, 1096–1098.

Potten, C.S., and Loeffler, M. (1990). Stem cells: attributes, cycles, spirals, pitfalls and uncertainties. Lessons for and from the crypt. Development *110*, 1001–1020.

Ramsköld, D., Luo, S., Wang, Y.-C., Li, R., Deng, Q., Faridani, O.R., Daniels, G.A., Khrebtukova, I., Loring, J.F., Laurent, L.C., et al. (2012). Full-length mRNA-Seq from single-cell levels of RNA and individual circulating tumor cells. Nat. Biotechnol. *30*, 777–782.

Reynolds, S.D., Hong, K.U., Giangreco, A., Mango, G.W., Guron, C., Morimoto, Y., and Stripp, B.R. (2000). Conditional clara cell ablation reveals a self-renewing progenitor function of pulmonary neuroendocrine cells. Am. J. Physiol. Lung Cell. Mol. Physiol. *278*, L1256–L1263.

Reynolds, S.D., Giangreco, A., Hong, K.U., McGrath, K.E., Ortiz, L.A., and Stripp, B.R. (2004). Airway injury in lung disease pathophysiology: selective depletion of airway stem and progenitor cell pools potentiates lung inflammation and alveolar dysfunction. Am. J. Physiol. Lung Cell. Mol. Physiol. *287*, L1256–L1265.

Rinkevich, Y., Lindau, P., Ueno, H., Longaker, M.T., and Weissman, I.L. (2011). Germ-layer and lineage-restricted stem/progenitors regenerate the mouse digit tip. Nature *476*, 409–413.

Sage, J., Miller, A.L., Pérez-Mancera, P.A., Wysocki, J.M., and Jacks, T. (2003). Acute mutation of retinoblastoma gene function is sufficient for cell cycle re-entry. Nature *424*, 223–228.

Salwig, I., Spitznagel, B., Vazquez-Armendariz, A.I., Khalooghi, K., Guenther, S., Herold, S., Szibor, M., and Braun, T. (2019). Bronchioalveolar stem cells are a main source for regeneration of distal lung epithelia *in vivo*. EMBO J. *38*, e102099.

Schindelin, J., Arganda-Carreras, I., Frise, E., Kaynig, V., Longair, M., Pietzsch, T., Preibisch, S., Rueden, C., Saalfeld, S., Schmid, B., et al. (2012). Fiji: an open-source platform for biological-image analysis. Nat. Methods *9*, 676–682.

Scialdone, A., Natarajan, K.N., Saraiva, L.R., Proserpio, V., Teichmann, S.A., Stegle, O., Marioni, J.C., and Buettner, F. (2015). Computational assignment of cell-cycle stage from single-cell transcriptome data. Methods *85*, 54–61.

Semenova, E.A., Nagel, R., and Berns, A. (2015). Origins, genetic landscape, and emerging therapies of small cell lung cancer. Genes Dev. *29*, 1447–1462.

Sheikh, A.Q., Misra, A., Rosas, I.O., Adams, R.H., and Greif, D.M. (2015). Smooth muscle cell progenitors are primed to muscularize in pulmonary hypertension. Sci. Transl. Med. *7*, 308ra159.

Sherr, C.J. (1996). Cancer cell cycles. Science *274*, 1672–1677.

Song, H., Yao, E., Lin, C., Gacayan, R., Chen, M.-H., and Chuang, P.-T. (2012). Functional characterization of pulmonary neuroendocrine cells in lung development, injury, and tumorigenesis. Proc. Natl. Acad. Sci. USA *109*, 17531–17536.

Stevens, T.P., McBride, J.T., Peake, J.L., Pinkerton, K.E., and Stripp, B.R. (1997). Cell proliferation contributes to PNEC hyperplasia after acute airway injury. Am. J. Physiol. *272*, L486–L493.

Susaki, E.A., Tainaka, K., Perrin, D., Kishino, F., Tawara, T., Watanabe, T.M., Yokoyama, C., Onoe, H., Eguchi, M., Yamaguchi, S., et al. (2014). Whole-brain imaging with single-cell resolution using chemical cocktails and computational analysis. Cell *157*, 726–739.

Sutherland, K.D., Proost, N., Brouns, I., Adriaensen, D., Song, J.-Y., and Berns, A. (2011). Cell of origin of small cell lung cancer: inactivation of Trp53 and Rb1 in distinct cell types of adult mouse lung. Cancer Cell *19*, 754–764.

Tabula Muris Consortium (2018). Single-cell transcriptomics of 20 mouse organs creates a Tabula Muris. Nature *562*, 367–372.

Tammela, T., Sanchez-Rivera, F.J., Cetinbas, N.M., Wu, K., Joshi, N.S., Helenius, K., Park, Y., Azimi, R., Kerper, N.R., Wesselhoeft, R.A., et al. (2017). A Wnt-producing niche drives proliferative potential and progression in lung adenocarcinoma. Nature *545*, 355–359.

Tirosh, I., Izar, B., Prakadan, S.M., Wadsworth, M.H., 2nd, Treacy, D., Trombetta, J.J., Rotem, A., Rodman, C., Lian, C., Murphy, G., et al. (2016). Dissecting the multicellular ecosystem of metastatic melanoma by single-cell RNA-seq. Science *352*, 189–196.

Treutlein, B., Brownfield, D.G., Wu, A.R., Neff, N.F., Mantalas, G.L., Espinoza, F.H., Desai, T.J., Krasnow, M.A., and Quake, S.R. (2014). Reconstructing lineage hierarchies of the distal lung epithelium using single-cell RNA-seq. Nature *509*, 371–375.

van den Brink, S.C., Sage, F., Vértesy, Á., Spanjaard, B., Peterson-Maduro, J., Baron, C.S., Robin, C., and van Oudenaarden, A. (2017). Single-cell sequencing reveals dissociation-induced gene expression in tissue subpopulations. Nat. Methods *14*, 935–936.

Wang, F., Flanagan, J., Su, N., Wang, L.-C., Bui, S., Nielson, A., Wu, X., Vo, H.-T., Ma, X.-J., and Luo, Y. (2012). RNAscope: a novel in situ RNA analysis platform for formalin-fixed, paraffin-embedded tissues. J. Mol. Diagn. *14*, 22–29.

Wapinski, O.L., Vierbuchen, T., Qu, K., Lee, Q.Y., Chanda, S., Fuentes, D.R., Giresi, P.G., Ng, Y.-H., Marro, S., Neff, N.F., et al. (2013). Hierarchical mechanisms for direct reprogramming of fibroblasts to neurons. Cell *155*, 621–635.

Weaver, M., and Krasnow, M.A. (2008). Dual origin of tissue-specific progenitor cells in Drosophila tracheal remodeling. Science *321*, 1496–1499.

Winslow, M.M., Dayton, T.L., Verhaak, R.G.W., Kim-Kiselak, C., Snyder, E.L., Feldser, D.M., Hubbard, D.D., DuPage, M.J., Whittaker, C.A., Hoersch, S., et al. (2011). Suppression of lung adenocarcinoma progression by Nkx2-1. Nature *473*, 101–104.

Wu, Y.E., Pan, L., Zuo, Y., Li, X., and Hong, W. (2017). Detecting activated cell populations using single-cell RNA-seq. Neuron *96*, 313–329.

Xing, Y., Li, A., Borok, Z., Li, C., and Minoo, P. (2012). NOTCH1 is required for regeneration of Clara cells during repair of airway injury. Stem Cells *30*, 946–955.

Xu, K., Nieuwenhuis, E., Cohen, B.L., Wang, W., Canty, A.J., Danska, J.S., Coultas, L., Rossant, J., Wu, M.Y.J., Piscione, T.D., et al. (2010). Lunatic Fringe-mediated Notch signaling is required for lung alveogenesis. Am. J. Physiol. Lung Cell. Mol. Physiol. *298*, L45–L56.

Yang, D., Denny, S.K., Greenside, P.G., Chaikovsky, A.C., Brady, J.J., Ouadah, Y., Granja, J.M., Jahchan, N.S., Lim, J.S., Kwok, S., et al. (2018). Intertumoral heterogeneity in SCLC is influenced by the cell type of origin. Cancer Discov. *8*, 1316–1331.

Yao, E., Lin, C., Wu, Q., Zhang, K., Song, H., and Chuang, P.-T. (2018). Notch signaling controls transdifferentiation of pulmonary neuroendocrine cells in response to lung injury. Stem Cells *36*, 377–391.

STAR★METHODS

KEY RESOURCES TABLE

REAGENT or RESOURCE	SOURCE	IDENTIFIER
Antibodies		
Chicken polyclonal anti-GFP	Abcam	Cat# ab13970; RRID:AB_300798
Goat polyclonal anti-Scgb1a1	Santa Cruz Biotechnology	Cat# sc-9772; RRID:AB_2238819
Goat polyclonal anti-Sox2	Santa Cruz Biotechnology	Cat# sc-17320; RRID:AB_2286684
Guinea pig polyclonal anti-CGRP	EuroProxima	Cat# 2263B-GP470-1
Mouse monoclonal anti-Foxj1 (with M.O.M.)	Thermo Fisher Scientific	Cat# 14-9965; RRID:AB_1548835
Rabbit polyclonal anti-CGRP	Enzo Life Sciences	Cat# BML-CA1134; RRID:AB_2068527
Rabbit monoclonal anti-Hes1 (with TSA)	Cell Signaling Technology	Cat# 11988S; RRID:AB_2728766
Rabbit polyclonal anti-RFP	Rockland	Cat# 600-401-379; RRID:AB_2209751
Rabbit polyclonal anti-Sftpc	MilliporeSigma	Cat# AB3786; RRID:AB_91588
Rat monoclonal anti-BrdU	Abcam	Cat# ab6326; RRID:AB_305426
Rat monoclonal anti-E-cadherin	Thermo Fisher Scientific	Cat# 13-1900; RRID:AB_2533005
Rat monoclonal anti-Ki67 conjugated to eFluor 570	Thermo Fisher Scientific	Cat# 41-5698-82; RRID:AB_11220285
Rat monoclonal anti-Ki67 conjugated to eFluor 660	Thermo Fisher Scientific	Cat# 50-5698-82; RRID:AB_2574235
Donkey polyclonal anti-Chicken IgY conjugated to Alexa Fluor 488	Jackson ImmunoResearch Labs	Cat# 703-545-155; RRID:AB_2340375
Donkey polyclonal anti-Goat IgG conjugated to Alexa Fluor 647	Thermo Fisher Scientific	Cat# A-21447; RRID:AB_2535864
Donkey polyclonal anti-Rat IgG conjugated to Alexa Fluor 647	Jackson ImmunoResearch Labs	Cat# 712-605-153; RRID:AB_2340694
Goat polyclonal anti-Guinea Pig IgG conjugated to Alexa Fluor 488	Thermo Fisher Scientific	Cat# A-11073; RRID:AB_2534117
Goat polyclonal anti-Guinea Pig IgG conjugated to Alexa Fluor 555	Thermo Fisher Scientific	Cat# A-21435; RRID:AB_2535856
Goat polyclonal anti-Guinea Pig IgG conjugated to Alexa Fluor 647	Thermo Fisher Scientific	Cat# A-21450; RRID:AB_2735091
Goat polyclonal anti-Mouse IgG1 conjugated to Alexa Fluor 647	Thermo Fisher Scientific	Cat# A-21240; RRID:AB_2535809
Goat polyclonal anti-Rabbit IgG conjugated to Alexa Fluor 488	Thermo Fisher Scientific	Cat# A-11034; RRID:AB_2576217
Goat polyclonal anti-Rabbit IgG conjugated to Alexa Fluor 555	Thermo Fisher Scientific	Cat# A-21429; RRID:AB_2535850
Goat polyclonal anti-Rabbit IgG conjugated to Alexa Fluor 647	Thermo Fisher Scientific	Cat# A-21245; RRID:AB_2535813
Goat polyclonal anti-Rabbit IgG conjugated to HRP	Vector Laboratories	Cat# PI-1000; RRID:AB_2336198
Rat monoclonal anti-CD31 conjugated to APC	BioLegend	Cat# 102409; RRID:AB_312904
Rat monoclonal anti-CD45 conjugated to APC	BioLegend	Cat# 103111; RRID:AB_312976
Rat monoclonal anti-F4/80 conjugated to APC	BioLegend	Cat# 123115; RRID:AB_893493
Rat monoclonal anti-CD326 conjugated to PE-Cy7	Thermo Fisher Scientific	Cat# 25-5791-80; RRID:AB_1724047
Chemicals, Peptides, and Recombinant Proteins		
Tamoxifen	MilliporeSigma	Cat# T5648
Naphthalene	Acros Organics	Cat# AC180902500
EdU (5-ethynyl-2′-deoxyuridine)	Thermo Fisher Scientific	Cat# A10044
BrdU (5-bromo-2′-deoxyuridine)	MilliporeSigma	Cat# B5002
Dibenzazepine (DBZ)	Tocris Bioscience	Cat #4489
Tween 80	MilliporeSigma	Cat# P1754

(*Continued on next page*)

Continued

REAGENT or RESOURCE	SOURCE	IDENTIFIER
(Hydroxypropyl)methyl cellulose	MilliporeSigma	Cat# H7509
Collagenase Type 4	Worthington Biochemical	Cat# CLS-4
Dispase	Corning	Cat# 354235
Trypsin-EDTA	Thermo Fisher Scientific	Cat# 25200056
DNase I	MilliporeSigma	Cat# 11284932001
UltraPure Low Melting Point Agarose	Thermo Fisher Scientific	Cat# 16520100
32% Paraformaldehyde Aqueous Solution	Electron Microscopy Sciences	Cat# 15714
Biotin Azide	Thermo Fisher Scientific	Cat# B10184
Streptavidin conjugated to Alexa Fluor 405	Thermo Fisher Scientific	Cat# S32351
Streptavidin conjugated to Alexa Fluor 647	Thermo Fisher Scientific	Cat# S21374
Tween 20	MilliporeSigma	Cat# P1379
Triton X-100	MilliporeSigma	Cat# X100
DAPI	Thermo Fisher Scientific	Cat# D1306
Mowiol 4-88	MilliporeSigma	Cat# 81381
DABCO (1,4-Diazabicyclo[2.2.2]octane)	MilliporeSigma	Cat# D2522
Quadrol (CUBIC 1)	MilliporeSigma; Susaki et al., 2014	Cat# 122262
Triethanolamine (CUBIC 2)	MilliporeSigma; Susaki et al., 2014	Cat# 90279
Critical Commercial Assays		
Mouse on Mouse (M.O.M.) Blocking Reagent	Vector Laboratories	Cat# MKB-2213
Click-iT EdU Alexa Fluor 488 Imaging Kit	Thermo Fisher Scientific	Cat# C10337
Click-iT EdU Alexa Fluor 647 Imaging Kit	Thermo Fisher Scientific	Cat# C10340
RNAscope Fluorescent Multiplex Reagent Kit	Advanced Cell Diagnostics	Cat# 320850
RNAscope Multiplex Fluorescent v2 Reagent Kit	Advanced Cell Diagnostics	Cat# 323100
TSA Plus Cyanine 5 and Flourescein System	PerkinElmer	Cat# NEL754001KT
Anti-CD31 MicroBeads (mouse)	Miltenyi Biotec	Cat# 130-097-418
Anti-CD45 MicroBeads (mouse)	Miltenyi Biotec	Cat# 130-052-301
C_1 Single Cell mRNA Seq IFC (10-17μm)	Fluidigm	Cat# 100-5760
C_1 Single Cell Reagent Kit for mRNA Seq	Fluidigm	Cat# 100-6201
SMARTer Ultra Low RNA Kit for the Fluidigm C_1 System	Clontech Laboratories	Cat# 634833
ERCC RNA Spike-In Mix	Thermo Fisher Scientific	Cat# 4456740
Nextera XT DNA Library Preparation Kit (96 samples)	Illumina	Cat# FC-131-1096
Nextera XT Index Kit (96 indexes, 384 samples)	Illumina	Cat# FC-131-1002
Agencourt AMPure XP	Beckman Coulter	Cat# A63880
Bioanalyzer High Sensitivity DNA Analysis Kit	Agilent Technologies	Cat# 5067-4626
Qubit dsDNA High Sensitivity Assay Kit	Thermo Fisher Scientific	Cat# Q32854
NextSeq 500 High Output v2 Sequencing Reagent Kit (150 cycles)	Illumina	Cat# FC-404-2002
Deposited Data		
RefSeq *Mus musculus* Transcript and Protein Database (mRNA_prot)	National Center for Biotechnology Information	RRID:SCR_003496; ftp://ftp.ncbi.nlm.nih.gov/refseq/M_musculus/mRNA_Prot
scRNA-seq of adult mouse NE and other cells	This paper	GEO:GSE136580
Experimental Models: Organisms/Strains		
Mouse: Ascl1^{CreERT2}: Ascl1$^{tm1.1(Cre/ERT2)Jejo}$	Jane Johnson, UT Southwestern; Kim et al., 2011	MGI:4452601; RRID:IMSR_JAX:012882
Mouse: CGRP^{CreERT2}: Calca$^{tm1.1(cre/ERT2)Ptch}$	Pao-Tien Chuang, UC San Francisco; Song et al., 2012	MGI:5460801

(*Continued on next page*)

Continued

REAGENT or RESOURCE	SOURCE	IDENTIFIER
Mouse: Lyz2^{Cre}: B6.129P2-Lyz2$^{tm1(cre)Ifo}$	Tushar Desai, Stanford University; Clausen et al., 1999	MGI:1934631; RRID:IMSR_JAX:004781
Mouse: Rosa26$^{LSL-ZsGreen}$: B6.Cg-Gt(ROSA) 26Sor$^{tm6(CAG-ZsGreen1)Hze}$	The Jackson Laboratory; Madisen et al., 2010	MGI:3809522; RRID:IMSR_JAX:007906
Mouse: Rosa26$^{LSL-tdTomato}$: B6.Cg-Gt(ROSA) 26Sor$^{tm9(CAG-tdTomato)Hze}$	The Jackson Laboratory; Madisen et al., 2010	MGI:3809523; RRID:IMSR_JAX:007909
Mouse: Rosa26$^{LSL-Rainbow}$: Gt(ROSA)26 Sor$^{tm1(CAG-EGFP,-mCerulean,-mOrange,-mCherry)Ilw}$	Irving Weissman, Stanford University; Rinkevich et al., 2011	MGI:5441200
Mouse: Rosa26$^{LSL-N1ICD-IRES-nEGFP}$: Gt(ROSA) 26Sor$^{tm1(Notch1)Dam}$	The Jackson Laboratory; Murtaugh et al., 2003	MGI:2684314; RRID:IMSR_JAX:008159
Mouse: Rb^{f}: B6;129-Rb1^{tm3Tyj}	Julien Sage, Stanford University; Sage et al., 2003	MGI:2450162; RRID:IMSR_JAX:008186
Mouse: p53^{f}: B6.129P2-Trp53^{tm1Brn}	Julien Sage, Stanford University; Jonkers et al., 2001	MGI:1931011; RRID:IMSR_JAX:008462
Oligonucleotides		
CGRP^{CreERT2} genotyping common forward primer (5 > 3) TCC AAA CCG TAT AGG CTA CAT GC	This paper	N/A
CGRP^{CreERT2} genotyping mutant reverse primer (5 > 3) CCC TGA ACA TGT CCA TCA GGT TC	This paper	N/A
CGRP^{CreERT2} genotyping wild type reverse primer (5 > 3) GGG GAA GTG GTG AAA GCA TTT TG	This paper	N/A
RNAscope probe to mouse Dll1 (Mm-Dll1-C2)	Advanced Cell Diagnostics	Cat# 425071-C2
RNAscope probe to mouse Jag1 (Mm-Jag1)	Advanced Cell Diagnostics	Cat# 412831
RNAscope probe to mouse Jag2 (Mm-Jag2-C3)	Advanced Cell Diagnostics	Cat# 417511-C3
RNAscope probe to mouse Notch2 (Mm-Notch2-C3)	Advanced Cell Diagnostics	Cat# 425161-C3
RNAscope probe to mouse Nrarp (Mm-Nrarp-C3)	Advanced Cell Diagnostics	Cat# 411771-C3
RNAscope probe to mouse Upk3a (Mm-Upk3a-C2)	Advanced Cell Diagnostics	Cat# 505891-C2
Software and Algorithms		
CASAVA v1.8.2	Illumina	RRID:SCR_001802; https://support.illumina.com/sequencing/sequencing_software/casava.html
kallisto v0.43.0	Lior Pachter; Bray et al., 2016	RRID:SCR_016582; https://pachterlab.github.io/kallisto/
RaceID2	Dominic Grün; Grün et al., 2016	RRID:SCR_017045; https://github.com/dgrun/StemID
jackstraw v1.0	Neo Chung; Chung and Storey, 2015	https://cran.r-project.org/web/packages/jackstraw/index.html
Cyclone	Florian Buettner; Scialdone et al., 2015	https://github.com/PMBio/cyclone
R v3.3.2	R Foundation for Statistical Computing	RRID:SCR_001905; https://www.r-project.org/
RStudio v1.0.136	RStudio	RRID:SCR_000432; https://www.rstudio.com/
gplots	Gregory Warnes	https://cran.r-project.org/web/packages/gplots/index.html
MATLAB	MathWorks	RRID:SCR_001622; https://www.mathworks.com/products/matlab.html
Fiji	SciJava; Schindelin et al., 2012	RRID:SCR_002285; https://fiji.sc/
Illustrator CS6	Adobe	RRID:SCR_010279; https://www.adobe.com/products/illustrator.html

LEAD CONTACT AND MATERIALS AVAILABILITY

Further information and requests for resources and reagents should be directed to and will be fulfilled by the Lead Contact, Mark A. Krasnow (krasnow@stanford.edu). All unique/stable reagents generated in this study are available from the Lead Contact without restriction.

EXPERIMENTAL MODEL AND SUBJECT DETAILS

Animals

Mouse lines used were tamoxifen-inducible, NE-specific knock-in Cre recombinase drivers *Ascl1*^{CreERT2} (also called *Mash1*^{CreERT2}) (Kim et al., 2011) and *CGRP*^{CreERT2} (also called *Calca*^{CreERT2}) (Song et al., 2012), constitutive knock-in Cre recombinase driver *Lyz2*^{Cre} (also called *LysM*^{Cre}) (Clausen et al., 1999), Cre-dependent single- or multi-color fluorescent reporters *Rosa26*$^{LSL\text{-}ZsGreen}$ (Ai6) (Madisen et al., 2010), *Rosa26*$^{LSL\text{-}tdTomato}$ (Ai9) (Madisen et al., 2010), and *Rosa26*$^{LSL\text{-}Rainbow}$ (Rinkevich et al., 2011), a Cre-dependent gain-of-function allele for *Notch1* also containing a nuclear green fluorescent reporter *Rosa26*$^{LSL\text{-}N1ICD\text{-}IRES\text{-}nEGFP}$ (Murtaugh et al., 2003), and Cre-dependent loss-of-function (“floxed”) alleles for *Rb1* (referred to as *Rb*^{f}) (Sage et al., 2003) and *Trp53* (referred to as *p53*^{f}) (Jonkers et al., 2001). Genotyping was performed on tail clips utilizing oligonucleotide primers reported previously for each strain, except *CGRP*^{CreERT2} for which new insertion-specific primers were designed (Key Resources Table). Adult mice aged 2-3 months were used in all experiments, with similar numbers of male and female mice analyzed and allocated to experimental groups. Sample sizes are given in Figure Legends, with 2-5 mice typically analyzed for each experimental condition and similar numbers for controls. Mice were maintained in 12hr light/dark cycle with food and water provided *ad libitum*. All animal husbandry, maintenance, and experiments were performed in accordance with Stanford University’s IACUC-approved protocols (APLAC 9780, 26676).

METHOD DETAILS

Tamoxifen induction of Cre recombination

Tamoxifen (MilliporeSigma T5648) stock solution (20mg/ml) was prepared by sonication in corn oil and stored at −20°C. Intraperitoneal (i.p.) injections of 4mg (200 μl) or 5mg (250 μl) of the tamoxifen stock solution were administered once or repeated every other day for the periods indicated in figure schemes and below. Tamoxifen induction of *Ascl1*^{CreERT2}*; Rosa26*$^{LSL\text{-}ZsGreen}$ and *Ascl1*^{CreERT2}*; Rosa26*$^{LSL\text{-}Rainbow}$ adult mice faithfully labeled adult NE cells: 3-5 weeks after induction all scored cells (n > 1000) in bronchial regions co-expressed the lineage label and NE marker CGRP. Tamoxifen injection schemes: Figure 1A (2 injections, 5mg each), Figure 3A (2x5mg), Figure 5G (1x4mg), Figure 5K (5x4mg), Figure 6A (2x4mg), Figure 7B (1x4mg), Figure S2A (1x4mg), Figure S3A (1x4mg), Figure S4B (1x4mg), Figure S4N (5x4mg), Figure S5A (1x4mg), Figure S5I (5x4mg), Figure S5K (1x4mg), Figure S6D (2x5mg), Figure S7A (1x4mg).

Airway injury with naphthalene

Naphthalene solution (50mg/ml) was prepared immediately before use by dissolving naphthalene (Acros Organics AC180902500) in corn oil by gentle rocking at room temperature for 30-60 minutes, then passed through a 0.2 μm filter (Nalgene 723-2520) to remove any undissolved solute. A single dose of naphthalene was delivered to adult mice by i.p. injection (275mg naphthalene per kg body weight) at least ten days after the final tamoxifen injection to allow tamoxifen clearance. Naphthalene-treated mice typically lost ~20%–25% of body weight in the three days after injury, then partially recovered to ~15%–20% loss at one week and ~0%–5% loss at three weeks. A minority of mice were refractory to naphthalene (i.e., did not lose weight, appeared alert and well groomed, and were active after injury) and were excluded from analysis. Larger doses (300mg naphthalene per kg body weight and above) resulted in 50%–100% lethality.

Cell proliferation analysis by EdU and BrdU labeling

Synthetic deoxyribonucleoside analogs EdU (Thermo Fisher A10044) and BrdU (MilliporeSigma B5002) were dissolved at 2mg/ml in sterile phosphate buffered saline (PBS, pH 7.4) and stored at −20°C. Adult mice were administered 200 μg (100 μl) doses i.p. daily as indicated in figure schemes. For experiments involving sequential EdU and BrdU labeling, nucleosides were delivered in alternate orders to separate cohorts of mice (Tables S2 and S5) to control for nucleoside-specific effects. Similar results obtained for both orders (greater fraction of NE cells positive for the nucleoside delivered after the first injury than after the second, large double-positive overlap, small fraction of NE cells positive only for the nucleoside delivered after the second injury), so aggregated data is reported in text and figures. No toxicity was apparent during or following the week-long daily dosing schemes. BrdU was detected in tissue cryosections by immunostaining as described below, except that immediately before immunostaining sections were subjected to antigen retrieval by submersion in pre-heated 10mM sodium citrate, 0.05% (v/v) Tween 20 (MilliporeSigma P1379) in distilled water (pH 6.0) for 15 minutes at 95°C. EdU was detected before or following immunostaining using click chemistry to covalently attach Alexa Fluor 647 azide to EdU alkyne incorporated into DNA during S phase of the cell cycle (Thermo Fisher C10340 Click-iT EdU Alexa Fluor 647 Imaging Kit). In some experiments, the Alexa Fluor 647 azide treatment of cryosections was replaced with treatment for one hour at room temperature with biotin azide (Thermo Fisher B10184, final concentration 30 μg/ml), to allow subsequent detection with Alexa

Fluor 405-conjugated streptavidin (Thermo Fisher S32351, final concentration 4 μg/ml in 0.3% (v/v) Triton X-100 (MilliporeSigma X100) in PBS). Dim and circumferential nuclear BrdU immunostaining that colocalized with the EdU signal was presumed to be cross-reaction of the anti-BrdU antibody for EdU and scored negative. With this filter, EdU single-positive cells were readily detected at abundances expected from the nucleoside delivery order, and for sequential injury (Figures 1I–1M) consistent results obtained using Ki67 immunostaining in place of BrdU (Figures S1M–S1Q).

Pharmacological inhibition of Notch signaling with dibenzazepine (DBZ)

A stock solution of 300mM DBZ (Tocris 4489) in DMSO was prepared and stored at 4°C with light protection. For injection, the DBZ stock solution (or DMSO alone for vehicle control) was diluted to 3mM DBZ with Tween 80 (MilliporeSigma P4780, final concentration 0.1% v/v) and (hydroxypropyl)methyl cellulose (MilliporeSigma H7509, final concentration 0.5% w/v), then administered i.p. to adult mice in daily DBZ doses of 30 μmol per kg body weight (10 μl per g body weight) for six consecutive days before harvesting on day seven for analysis.

Immunohistochemistry

Mice were euthanized by CO_2 asphyxiation and lungs dissected immediately following perfusion with ~5ml PBS into the right cardiac ventricle and intratracheal inflation with ~2ml of 2% (w/v) low melting point agarose (Thermo Fisher 16520100) in PBS. Lungs were fixed in 4% (v/v) paraformaldehyde (PFA) for six hours at 4°C with gentle rocking, prepared fresh by dilution of a 32% stock solution (Electron Microscopy Sciences 15714) in PBS.

For cryosections, lungs were dehydrated in 30% (w/v) sucrose in PBS overnight at 4°C before embedding in optimum cutting temperature compound (OCT, Tissue-Tek 4583) and storage at −80°C. Coronal sections (20 μm) were prepared using a cryostat (Leica Biosystems CM3050 S) and cryosections were adhered to Superfrost Plus slides (VWR 48311-703), dried at room temperature for 15-60 minutes, and washed twice at room temperature with gentle rocking for five minutes each in 0.3% (v/v) Triton X-100 in PBS. Sections were incubated for one hour at room temperature in either 5% (v/v) normal goat (Jackson ImmunoResearch 005-000-121) or donkey serum (Jackson ImmunoResearch 017-000-121) in 0.3% Triton X-100 PBS (cryoblock solution), then incubated overnight at 4°C in cryoblock solution containing unconjugated primary antibodies (Key Resources Table) in a humid chamber. For Foxj1 immunostaining (which utilizes a mouse-derived primary antibody), cryoblock solution also contained "Mouse on Mouse" Mouse Ig Blocking Reagent (Vector Laboratories MKB-2213, diluted 1:35) during the blocking step, which was washed out prior to antibody incubation in normal cryoblock. The following day, sections were washed three times for five minutes each in 0.3% Triton X-100 PBS, then incubated for one hour at room temperature in cryoblock solution containing Alexa Fluor-conjugated secondary antibodies (Key Resources Table) and DAPI (Thermo Fisher D1306, 100ng/ml). Stained sections were finally washed twice for five minutes each in 0.3% Triton X-100 PBS and once for five minutes in PBS. Washed sections were mounted on coverslips (VWR 48393-106) using Mowiol 4-88 (MilliporeSigma 81381) with DABCO antifade (MilliporeSigma D2522) as the mounting medium, prepared according to http://cshprotocols.cshlp.org/content/2006/1/pdb.rec10255 except the centrifugation step. Mounted specimens were stored at 4°C until microscopy.

For Hes1 immunostaining of cryosections, tyramide signal amplification (TSA) was performed using the PerkinElmer TSA Plus Cyanine 5 (Cy5) detection kit (PerkinElmer NEL754001KT). Sections stained with rabbit anti-Hes1 primary antibody (Key Resources Table) were incubated with horse radish peroxidase (HRP)-conjugated anti-rabbit IgG (Key Resources Table), washed, then incubated with Cy5-conjugated tyramide (prepared according to manufacturer's instructions, then diluted 1:100 in amplification diluent) for three minutes at room temperature. Slides were then washed again before DAPI staining, mounting, and confocal microscopy.

For thick, "whole-mount" sections, PFA-fixed lungs were stored at 4°C in PBS and kept protected from light until sectioning. Lung coronal sections (500 μm) were prepared from the left or right cranial lobe with a vibrating blade microtome (Leica Biosystems VT1000 S). Sections were incubated overnight at 4°C with gentle rocking in either 5% normal goat or donkey serum in 0.5% Triton X-100 PBS (whole mount block solution), then incubated in whole mount block solution containing unconjugated rabbit anti-CGRP primary antibody (Key Resources Table) for 4-6 days at 4°C with gentle rocking and light protection. Primary-stained slices were washed in 0.5% Triton X-100 PBS 5-6 times for one hour each at room temperature with gentle rocking, then incubated in whole mount block solution containing Alexa Fluor-conjugated anti-rabbit IgG secondary antibodies (Key Resources Table), Alexa Fluor-conjugated streptavidin (Thermo Fisher S32351/S21374, 4 μg/ml) to detect lung epithelium endogenous biotin stores (Kuhn, 1988), and DAPI (100ng/ml) for 2-3 days at 4°C with gentle rocking and light protection. Secondary-stained slices were washed again as above then optically cleared using the CUBIC method (Susaki et al., 2014), comprising a three hour incubation in CUBIC 1 reagent at room temperature with gentle rocking and storage in CUBIC 2 at 4°C until confocal microscopy. With the exception of nuclear EGFP encoded by the *Rosa26*$^{LSL\text{-}N1ICD\text{-}IRES\text{-}nEGFP}$ allele and tdTomato detection in conjunction with smFISH (see below), all genetically encoded fluorophores were detected by endogenous fluorescence rather than by immunostaining.

Single molecule fluorescence *in situ* hybridization (smFISH)

Mice were euthanized and lungs were dissected and prepared for *in situ* hybridization with RNAscope (Advanced Cell Diagnostics, ACD) (Wang et al., 2012) as for immunostaining, except that nuclease-free buffers were used for all incubations and washes. Coronal cryosections (12 μm) were adhered to Superfrost Plus slides, dried at room temperature for 15-30 minutes, and pretreated by incubating slides in 1X Target Retrieval buffer (ACD 322000) at 95°C for five minutes, washed twice with nuclease-free water and once

with 100% ethanol for two minutes each, then treated with Protease III (ACD 322281) for 30 minutes at 40°C. Slides were then washed twice with nuclease-free water before proceeding with probe hybridization (Key Resources Table) for two hours at 40°C and fluorescent amplification of puncta. For *Notch2* detection, smFISH signal was detected with or without enzymatic amplification of fluorescent puncta according to ACD instructions (with, RNAscope Multiplex Fluorescent Reagent Kit v2 (ACD 323100) with TSA Plus fluorescein (PerkinElmer NEL754001KT); without, RNAscope Multiplex Fluorescent Reagent Kit (ACD 320850) with Amp 4 Alt B-FL and Atto 647 fluorophore). Similar results obtained with or without amplification so aggregated data is reported (representative images in Figures 7C and S7B are without amplification). By contrast, detection of *Dll1*, *Jag1*, *Jag2*, *Nrarp*, and *Upk3a* (Figure S4) all included enzymatic amplification with TSA Plus fluorescein or Cy5 according to ACD instructions. In cases where no C1 probe was utilized, C2 and/or C3 probes were delivered in probe diluent (ACD 300041). Following completion of the RNAscope protocol, tdTomato was detected by immunostaining using rabbit anti-RFP primary and anti-rabbit Alexa Fluor 555 secondary antibodies (Key Resources Table), EdU by click chemistry with Alexa Fluor 488 azide (Thermo Fisher C10337 Click-iT EdU Alexa Fluor 488 Imaging Kit), and cell nuclei with DAPI before mounting coverslips with Mowiol 4-88 with DABCO and proceeding to confocal microscopy. For quantification of *Notch2* expression in NE cells, puncta were scored only if signal was detected in multiple adjoining pixels in three dimensions (i.e, within an optical section or in consecutive optical sections) to avoid tallying spurious puncta possibly present due to imperfect camera function. EdU^+ $Notch2^-$ cells were scored as adjacent to an EdU^+ $Notch2^+$ cell if the cells directly contacted (in three dimensions) or were "connected" via a continuous chain of intervening EdU^+ $Notch2^-$ cells.

Microscopy and imaging

Cryosections (12-20 μm) were imaged using a Zeiss LSM 780 laser scanning confocal microscope with an inverted 40X oil immersion objective (Carl Zeiss AG, NA = 1.4). Optical sections were collected at 0.5 μm resolution through the z plane (dorsoventral axis of lung). Thick sections were placed in inverted coverglass chambers (Nunc Lab-Tek 155361), mounted with coverslips (VWR 89015-724) using CUBIC 2 as the mounting medium, and imaged using a Zeiss LSM 780 laser scanning confocal microscope with either an inverted 25X oil immersion objective (Carl Zeiss AG, NA = 0.8) or a 10X air objective (Carl Zeiss AG, NA = 0.45). Optical sections were collected at 2 μm (25X) or 5 μm (10X) resolution. Images shown in figures are either single optical sections or maximum intensity projections of image stacks, but in all cases image feature quantifications represent cumulative counts through multiple optical sections. For cryosections, serial sections were generally visually inspected to ensure that no apparent differences in the various feature patterns reported were observed, however for consistency serial sections of the same NEB were excluded from quantifications. Note that, in addition to NEBs (> 15 NE cells), NE cells also organize during mouse lung development into mini-clusters (~5-10 NE cells) and singletons scattered within the proximal airway epithelium (Kuo and Krasnow, 2015; Noguchi et al., 2015), although neither population was investigated in the current study. Fiji (Schindelin et al., 2012) was used to color, overlay, adjust brightness and contrast, and add scale bars to z stack, single optical section, and maximum intensity projection images. The Cell Counter software plugin was used to aid manual counts of features of interest. Illustrator CS6 (Adobe) was used to rotate, crop, and annotate images.

Simulations of NE proliferation after injury

We simulated NEB dynamics after injury using a custom MATLAB algorithm. For a given NEB of n cells, the initial cell "colors" (indicating fluorescent protein expression from the Rainbow allele) were determined using probabilities derived from the empirical color distribution of uninjured NEBs ($p_{mCerulean} = 0.54$, $p_{mOrange} = 0.18$, $p_{mCherry} = 0.10$, $p_{EGFP} = 0.18$). Using these probabilities, the color of each cell was selected using the multinomial distribution. From n, we assumed there was a probability p that each cell was a progenitor cell (a cell that could possibly divide). The temporal dynamics of progenitor cells were determined as follows. We assumed that most progenitor cells were enforced to divide, based on the observation from sequential injury experiments that, if a cell divided in either injury round, there was a high chance that it divided in the first round (i.e., very few new cells divided uniquely in the second round). To implement this, we stipulated that there was a probability r that a given cell would divide in the first time step of the simulation. Progenitor cells that did not divide in the first time step could still divide in later time steps. We assumed that, once a cell began dividing, it could not divide again for 12 hours. Cells that were eligible to divide (had not divided in the last 12 hours) divided with a probability per unit time q. The simulation proceeded in ten minute time steps. NEB dynamics were followed for a total time T. We simulated N = 690 NEBs, taking initial NEB size, n, from the empirical uninjured NEB size distribution.

We studied the parameter space:

$$0.05 < p < 0.25$$

$$0.0003 < q < 0.0243\,[\mathrm{hr}^{-1}]$$

$$40 < T < 90\,[\mathrm{hr}]$$

$$0.8 < r < 1$$

We fit simulation results to the empirically determined fraction of cells per color that end the injury response period as EdU^+ (i.e., the union of NE "parent" and "daughter" cells). We found the best fit to be p = 0.17, $q = 0.0003hr^{-1}$, $T = 45hr$, $r = 0.8$, informing a simple model in which NE progenitor cells comprise 17% of the total and usually only divide once (and at most three times) during the injury response period.

NE cell purification by Fluorescence-Activated Cell Sorting (FACS)

To purify live NE cells for scRNA-seq profiling, adult *Ascl1*^{CreERT2}; *Rosa26*$^{LSL\text{-}ZsGreen}$ or *CGRP*^{CreERT2}; *Rosa26*$^{LSL\text{-}ZsGreen}$ mice (roughly equal numbers of 2-3 month old male and female littermates) were administered a single 4mg i.p. injection of tamoxifen, then 4-7 days later euthanized by CO_2 asphyxiation, perfused with ~2ml PBS into the right cardiac ventricle, and lungs dissected and pooled (6-10 lungs per collection round) to insure sufficient numbers of labeled NE cells for sorting. (The *CGRP*^{CreERT2} driver is homozygous viable and fertile so was preferentially used over the *Ascl1*^{CreERT2} driver for breeding convenience.) Whole lungs excluding the trachea were dissociated by cutting them into small pieces with surgical scissors then enzymatically digesting the pieces in Hank's balanced salt solution (HBSS) containing 1mg/ml collagenase type 4 (Worthington CLS-4), 5U/ml dispase (Corning 354235), and 0.025% (v/v) trypsin-EDTA (Thermo Fisher 25200056) for one hour at 37°C with rotation, with intermittent pipette trituration (Winslow et al., 2011). Following digestion, enzymes were quenched by adding two-fold excess volume of PBS containing 10% (v/v) fetal bovine serum (FBS, Thermo Fisher 10082147), 20 μg/ml DNase I (MilliporeSigma 11284932001), and 2mM EDTA. Thereafter, samples were kept continually on ice or at 4°C and added solutions were chilled and contained 2mM EDTA to prevent Ca^{2+}-mediated cell adhesion. Digested suspensions were pressed through a 40 μm cell strainer (Corning 352340) and incubated in red blood cell (RBC) lysis buffer (155mM NH_4Cl, 140mM $NaHCO_3$, 1mM EDTA in distilled water, pH 7.3) for five minutes on ice, after which individual genotype (but not gender) matched lungs were combined into a single sample. Five minute centrifugations (200 x *g*) were performed between each step and the cell-free supernatants removed by vacuuming. RBC-lysed cell suspensions were depleted for endothelial cells and leukocytes using anti-CD31 (also called *Pecam1*, Miltenyi Biotec 130-097-418) and anti-CD45 (*Ptprc*, Miltenyi Biotec 130-052-301) decorated magnetic microbeads and MACS separation columns (Miltenyi Biotec 130-042-401), according to the manufacturer's instructions. PBS with 2% FBS and 2mM EDTA (FACS buffer) was used as the suspension solution for magnetic labeling and for cell application onto columns. Endothelial/leukocyte-depleted cell suspensions were stained with allophycocyanin (APC)-conjugated anti-CD31, anti-CD45, and anti-F4/80 (also called *Adgre1* or *Emr1*) primary antibodies, each at 1:800 dilution in FACS buffer, and phycoerythrin and cyanine 7 (PE-Cy7)-conjugated anti-CD326 (also called *Epcam*) at 1:400 dilution for 30 minutes at 4°C (Key Resources Table). Finally, stained cell suspensions were washed twice for five minutes each in FACS buffer to remove residual unbound antibodies, then were resuspended in FACS buffer containing 1 μg/ml DAPI as a live/dead cell indicator before proceeding to FACS. Cell sorting was performed in the Stanford Shared FACS Facility using an Aria II flow cytometer (BD Biosciences) with a 100 μm nozzle. Unstained lung cell suspensions from littermates carrying the *Rosa26*$^{LSL\text{-}ZsGreen}$ reporter without a Cre recombinase allele were used as negative gating controls for each fluorophore. Approximately 500-3,000 $DAPI^-$ APC^- $PE\text{-}Cy7^+$ $ZsGreen^+$ live NE cells were collected into FACS buffer per sorting session, and in some cases (see Table S3) $DAPI^-$ APC^- $PE\text{-}Cy7^+$ $ZsGreen^-$ live non-NE epithelial cells were also collected as controls. Because the majority of non-NE epithelial cells captured tended to be alveolar type 2 (AT2) cells, in two isolation rounds a single *Lyz2*^{Cre}; *Rosa26*$^{LSL\text{-}ZsGreen}$ adult (2 months old) mouse was used in order to de-enrich for AT2 cells (in addition to macrophages and neutrophils, *Lyz2* is also a specific marker for AT2 cells) (Desai et al., 2014). All lung cell preparation and staining steps were performed identically as before, and $DAPI^-$ APC^- $PE\text{-}Cy7^+$ $ZsGreen^-$ live non-AT2 epithelial cells were collected by FACS.

Microfluidic single cell capture and cDNA library preparation

Single cells from FACS-sorted suspensions were captured on a medium-sized (10-17 μm cell diameter) integrated fluidic circuit (IFC, Fluidigm 100-5760) using the Fluidigm C_1 system and reagent kit (Fluidigm 100-6201) according to the manufacturer's instructions, similar to as previously described (Treutlein et al., 2014). After IFC priming, cells were loaded at a concentration of 400-800 cells/μl in a 6 μl volume (2,400-4,800 cells loaded per IFC), which consisted of a 2:3 volumetric ratio of suspended cells in FACS buffer and C_1 suspension reagent, respectively. In cases where sufficient NE cells were acquired during sorting so they could be loaded as a pure population, this was performed, otherwise non-NE epithelial cells were mixed in to achieve the total desired cell number (this occurred only in cases when NE cells were collected after labeling with *Ascl1*^{CreERT2} and not with *CGRP*^{CreERT2}). After loading, phase contrast and green fluorescence photomicrographs were taken of each of the 96 cell capture sites to assess the presence, number, viability, and ZsGreen status of the cell(s) in each site using an epifluorescence microscope outfitted with an automated stage. In cases of low capture efficiency and if additional cells were available, a second identical round of cell loading and microscopy was performed to capture and identify additional cells. Following image acquisition, captured cells were lysed, poly-adenylated mRNAs captured, and cDNAs prepared by reverse transcription and 21 cycles of PCR amplification on-chip using Smart-Seq (SMARTer Ultra Low RNA and Advantage 2 PCR kits, Clontech 634833) (Ramsköld et al., 2012). ERCC spike-in transcripts (Thermo Fisher 4456740) (Jiang et al., 2011) were added to the cell lysis mixture from the manufacturer's stock at a final dilution of 1:40,000, and processed in parallel with cellular mRNAs. The next day, cDNA pools were collected off IFCs and their concentration and size distribution determined using a capillary electrophoresis-based fragment analyzer (Advanced Analytical). Samples derived from single, live cells (based on photomicrographs collected on-chip prior to lysis) and containing high quality cDNA (> 0.05ng/μl total cDNA in the 300-5,000 bp range) were used to construct sequencing libraries in 96-well format using the Nextera XT DNA Library Preparation

kit (Illumina FC-131-1096) and Index Adapters (Illumina FC-131-1002) according to the Fluidigm C_1 protocol. cDNA inputs were normalized by dilution across all samples prior to tagmentation. During library preparation, cDNA pools underwent an additional 12 cycles of PCR amplification whereupon unique barcodes were attached and final products were purified using Agencourt AMPure XP beads (Beckman Coulter A63880).

Single cell mRNA sequencing

Before sequencing, single cell cDNA libraries were quantified by Bioanalyzer using the High Sensitivity DNA kit (Agilent 5067-4626), as well as fluorometrically using a Qubit 2.0 Fluorometer (Thermo Fisher) with the Qubit double-stranded DNA High Sensitivity Assay kit (Thermo Fisher Q32851). Up to 96 single cell libraries were pooled from 1-3 individual IFCs and sequenced together on one lane of a NextSeq 500 (Illumina) using the High Output v2 kit (150 cycles, Illumina FC-404-2002) to generate 75bp paired-end reads at a mean sequencing depth of 6.9 million fragments (paired reads) per cell. In total, 238 cells from nine IFCs were sequenced in six independent runs. CASAVA 1.8.2 (Illumina) was used for base calling, to assign fragments to the appropriate cell based on Nextera XT unique barcodes (demultiplexing), and to generate *fastq* files. Fragments were computationally processed to trim exogenous sequences added during library preparation and remove short, low complexity, and overrepresented sequences as previously described (Ooi et al., 2017). Groomed fragments were aligned to the NCBI RefSeq mouse transcriptome (mouse.rna.fna.gz downloaded from ftp://ftp.ncbi.nlm.nih.gov/refseq/M_musculus/mRNA_Prot on April 7, 2014), modified to exclude model (XR_/XM_) ascensions and to include ERCC (acquired from the manufacturer) and *ZsGreen* (acquired from the pZsGreen1-N1 vector (Clontech 632448)) sequences, using kallisto (Bray et al., 2016) with default settings. As an initial quality control, cells with fewer than 300,000 aligned endogenous fragments (total aligned fragments, retrieved from the *est_counts* kallisto output subtracting those mapped to ERCCs) were rejected from further analysis, resulting in exclusion of 12 cells (5%). Next, ERCC-mapped fragments were removed from each cell and transcripts per million (TPM) were calculated by first dividing aligned endogenous fragments by the effective transcript length discovered in that cell (retrieved from the *eff_length* kallisto output), then dividing by the parental cell's total aligned endogenous fragments and multiplying by one million. Finally, TPM values from splice isoforms belonging to the same gene were summed, thus collapsing the full expression table from 32,887 transcripts to 24,173 genes. As a second quality control, a heatmap representing expression ($\log_2$ TPM+1) of curated housekeeping genes (Tirosh et al., 2016) was visually inspected to identify cells with abnormally low or erratic patterns (indicating the cell was unhealthy at the time of lysis), leading to exclusion of 1 cell (0.4%). Ultimately, 225 cells passed both quality controls and were analyzed further, including 100 that were identified from cell capture photomicrographs as ZsGreen$^+$ and hence NE in origin.

Single cell mRNA sequencing analysis

Following alignment, all computational analyses were performed in R v3.3.2 (''Sincere Pumpkin Patch'') using the RStudio graphical user interface (v1.0.136). To investigate measurement sensitivity and precision, observed ERCC ''expression'' ($\log_2$ TPM_{ERCC}+1, where TPM_{ERCC} values are calculated without contribution from endogenous fragments) was compared to known spike-in copy number ($\log_2$ copy number per cell) acquired from concentrations supplied by the manufacturer corrected for dilution and reaction volume, as performed previously (Treutlein et al., 2014). A log-log linear fit was made to the mean expression ($\log_2$ mean TPM_{ERCC}+1) of each of the 92 ERCCs across all cells, leading to an estimation of TPM $\approx$ 66 to correspond to 1 transcript copy per cell (on average) and selection of TPM = 10 as a suitable cutoff to reliably declare a gene ''expressed'' in any one cell. Linear fitting was performed using the *lm* function from the base *stats* package in R. Cell type classification was performed using RaceID2 (Grün et al., 2016), wherein gene expression was represented as TPM+1 (excluding ERCCs, non-log transformed) and included all 13,023 genes expressed (TPM > 10) in at least any 5 of the 225 total cells (2.5%). No additional data filtering or normalization was performed prior to analysis. All default parameters were used with the following exceptions: *clustnr = 10, boonr = 100* (*clustexp* function); *max_iter = 1e3* (*comptsne* function); *outminc = 25, outlg = 3, probthr = 1e-4* (*findoutliers* function). For principal component analysis (PCA), genes expressed (TPM > 10 in at least any 3 NE cells) highly variably within the 100 ZsGreen$^+$ NE cells (based on cell capture photomicrographs) were first identified by generating a ratio of each gene's measured coefficient of variation (CV, defined as standard deviation TPM+1/mean TPM+1) to that expected based on a log-log quadratic fit of housekeeping genes across a wide range of expression means (quadratic fit calculated using the *lm* and *poly* functions in the base *stats* package). Genes were ranked by this ratio and the top 2% (230 genes) were selected for inclusion in PCA. In addition, 23 genes exhibiting both high expression ($\log_2$ mean TPM+1 > 10) and at least mild variability ($\log_2 CV_{measured}$ / $\log_2 CV_{expected}$ > 1.5) were also selected, in order to account for characteristically lower variation in highly expressed genes (Grün and van Oudenaarden, 2015). The unique intersect of both lists totaled 244 genes, which were selected for inclusion in PCA. PCA was performed on gene-centered and scaled expression values ($\log_2$ TPM+1) in NE cells using the *prcomp* function from the base *stats* package. Significance values for the percent of variance explained per component were calculated using the *permutationPA* function from the jackstraw package (Chung and Storey, 2015) with parameters *B = 1e3* and *threshold = 5e-2*, yielding 20 components with $p < 0.05$. Significance values for gene loadings within each component were calculated using the *jackstraw* function with parameters *r = 20* and *B = 1e3*, with additional multiple hypothesis correction using the Benjamini-Hochberg procedure to account for the total number of components investigated (20). Genes were considered significantly loaded if $p < 0.05$. Heatmaps were generated using the *heatmap.2* function from the *gplots* package, with expression represented as $\log_2$ TPM+1, dissimilarity calculated as Euclidean distance, and gene (i.e., row) and/or cell (i.e., column) hierarchical clustering performed using Ward's method. Custom gene lists for lung markers, Notch pathway components, and neurosensory/secretory

character were compiled manually from literature review. Feature plots were generated in tSNE and PCA space using custom scripts to allocate an individual gene's expression distribution (log_2 TPM+1) across cells into evenly sized bins; thus, not all bins need contain an equal number of cells. Cells were then plotted with overlapping points piled in order of ascending expression level. Spearman correlations were calculated using the *cor* function from the base *stats* package, with expression (TPM) values less than 10 set to 0 to reduce the contribution of cells with very low expression. For cell cycle phase assignment, Cyclone (Scialdone et al., 2015) was used with NE gene expression (log_2 TPM+1) as input and default settings.

Analysis of additional mouse NE cell scRNA-seq profiles

The additional NE cell scRNA-seq is from a study of NE cell development to be described elsewhere (C.S.K., S. Darmanis, N. Almanzar, Y.O., S.R. Quake, and M.A.L., unpublished data). Briefly, the 160 adult NE and transitional cells (Figure S3J) were isolated from adult (90 and 120 day old) *Ascl1*^{CreERT2}*; Rosa26*$^{LSL\text{-}ZsGreen}$ mice after tamoxifen induction, and individual cells were flow sorted directly into cell lysis buffer (as in Tabula Muris Consortium et al., 2018) rather than captured on a microfluidic (Fluidigm C_1) chip as above. cDNA libraries were generated and amplified manually by Smart-seq2 (Picelli et al., 2013), sequenced (Illumina NextSeq 500, 75 bp paired-end reads), and aligned using STAR (Dobin et al., 2013). Unhealthy cells and poor quality profiles (< 500 unique genes detected) and presumed cell doublets (> 5,000 unique genes detected) were excluded. EpCAM$^+$ ZsGreen$^+$ cells that were also *Calca*$^+$ and/or *Resp18*$^+$ (CPM > 10) were defined as NE (or NE-derived). Principal component analysis was performed as above.

QUANTIFICATION AND STATISTICAL ANALYSIS

Quantification of NEB size, outgrowths, and cell dispersals

NEB outgrowth size (Figure 3G) was measured in thick (500 μm) z stack images of the lungs of *Ascl1*^{CreERT2}*; Rosa26*$^{LSL\text{-}Rainbow}$ mice. CGRP immunofluorescence was used to identify NEBs, and Rainbow fluorophores (mCerulean, mOrange, mCherry) were used to identify the associated NE clonal lineages. Outgrowths were defined as coherent, monochromatic patches of Rainbow fluorescence that extended beyond the NEB (CGRP$^+$) boundary. Because of the preponderance of mCerulean recombination in NE cells, mCerulean-labeled lineages were excluded from analysis to minimize the possibility of counting oligoclonal outgrowths originating from more than one mCerulean-labeled clone from the same parental NEB, which would appear monochromatic. NEBs were first identified in optical sections by converting CGRP immunofluorescence to a binary mask using a threshold signal intensity value of 1000. A morphological dilation was used to ensure each NE cell nucleus was included, and the dilated mask was applied to corresponding mCerulean, mOrange, and mCherry channels to colocalize CGRP/Rainbow double-positive pixels and exclude them from quantification. The mask was followed by a morphological opening to remove any remaining small pixel islands. The number of remaining objects in each Rainbow channel was found using a three-dimensional connectivity of 26 neighboring pixels, and each object was subsequently considered an individual outgrowth. The number of CGRP$^-$ cells in each outgrowth was estimated by the size of the outgrowth (number of pixels), assuming a standard cell size of 75 pixels, defined using CGRP immunofluorescence. The fraction of bronchial epithelial surface from NEBs and their outgrowths (Figure S2F) was calculated by converting ZsGreen fluorescence from the lungs of *Ascl1*^{CreERT2}*; Rosa26*$^{LSL\text{-}ZsGreen}$ mice to a binary mask, and dividing the total number of ZsGreen$^+$ pixels by the number of biotin$^+$ pixels (also converted to a binary mask) within regions identified as bronchial branches in maximum intensity projections of thick z stack images. NEB sizes and dispersal and outgrowth frequencies (Figures 6R, 6S, S5N, and S6C) were measured in the lungs of *Ascl1*^{CreERT2}*; Rosa26*$^{LSL\text{-}ZsGreen}$ mice in a higher throughput format using just the green fluorescence channel in stereoscopic images to assess NE cells and their lineage (as in Figures 6N, 6O, S6A, and S6B). For these, two-dimensional, low-power (8X magnification) green fluorescence photomicrographs were taken of thick lung slices using an upright stereomicroscope (Leica Biosystems MZ16 FA). A signal intensity threshold of 125 was applied to all images to remove background noise and the number of connected components was identified using two-dimensional connectivity of 8 pixels, excluding components of size 1 (individual pixels). Components with size > 299 pixels were considered outgrowths while those > 26 pixels and < 151 pixels were considered normal NEBs (i.e., without associated outgrowths). Size thresholds were defined using reference images of uninjured lungs.

Dispersed NEBs were identified in three-dimensional z stacks and two-dimensional photomicrographs of the lungs of *Ascl1*^{CreERT2}*; Rosa26*$^{LSL\text{-}Rainbow}$ and *Ascl1*^{CreERT2}*; Rosa26*$^{LSL\text{-}ZsGreen}$ mice by visual assessment and comparison to reference images from uninjured lungs. For satellite cell distance measurements (Figures 2D and 2E), the center of each NEB was first defined manually as a single point in the image stack. Cells double-positive for CGRP immunofluorescence and the NE lineage marker were then identified as "satellite cells" if they appeared as either single or small groups of cells (~4-8) segregated sufficiently far from the nearby parental NEB in a morphological pattern distinct from uninjured NEBs, and were defined spatially as a single central point in the nucleus. Single segregated cells in the vicinity of NEBs were not scored due to potential confound by normal solitary NE cells. The Euclidean distance was then measured between the center of the NEB and the central point of the satellite cell.

Statistical analysis

Sample sizes (n) including the number of NE cells, number of NEBs, and number of mice analyzed are reported for each experiment in the manuscript, including Results, Figures, and Figure Legends. Box-and-whisker plots show median, interquartile range (IQR, box), and distribution range within 1.5 times the IQR (whiskers), with data points overlaid. Experimenter (Y.O.) was blinded to order of proliferation tracer (EdU, BrdU) administration during analysis of sequential injury and injury followed by Rb/53 deletion experiments

(Figures 1I–1M and 6I–6M). Blinding to injury status was not possible due to the strong behavioral effects on mice as well as anatomical and cellular effects on bronchial epithelium of naphthalene and DBZ treatments.

Statistical tests producing p values shown in figures were performed in R. Pairs of vector distributions were compared using the nonparametric two-sided Mann-Whitney *U* test (also known as the Wilcoxon rank-sum test), implemented using the *wilcox.test* function from the base *stats* package. Overlap between distributions (e.g., EdU/BrdU) was investigated using the hypergeometric test (also known as the one-tailed version of Fisher's exact test), implemented using the *phyper* function from the base *stats* package. Frequencies of occurrence for various biological features were compared using the two-sided binomial test, implemented using the *binom.test* function from the base *stats* package. Binomial fits were produced using the *dbinom* function from the base *stats* package, with empirically determined means and sample sizes as inputs. Chi-squared values were produced using the *chisq.test* function from the base *stats* package. P values were corrected for multiple hypothesis testing when appropriate using the Benjamini-Hochberg procedure. Astrices are used to denote significance, with * $p < 0.05$, ** $p < 10^{-2}$, and *** $p < 10^{-3}$.

DATA AND CODE AVAILABILITY

The scRNA-seq dataset generated during this study is available at Gene Expression Omnibus (GEO: GSE136580) with associated metadata file available as Table S3.

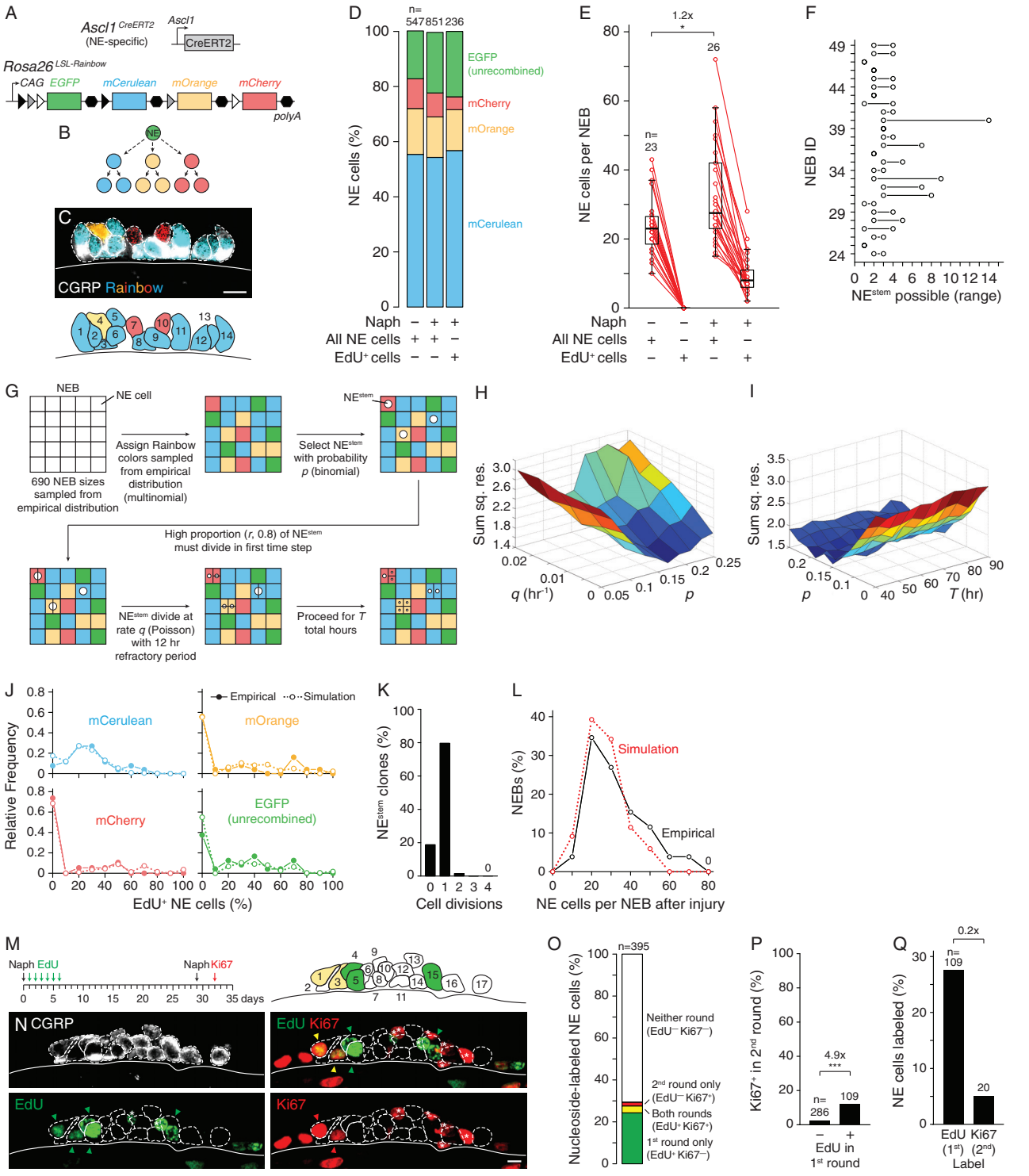

Figure S1. NE Multicolor Labeling and Proliferation after Naphthalene Injury, Related to Figure 1

(A) Schematics of *Ascl1*^{CreERT2} and *Rosa26*$^{LSL\text{-}Rainbow}$ knock-in alleles used for NE clonal labeling (Kim et al., 2011; Rinkevich et al., 2011). CreER^{T2} is expressed in NE cells and activated by tamoxifen, which induces nuclear translocation of the fusion protein by binding to the estrogen receptor ligand-binding domain (ER^{T2}). CreER^{T2} catalyzes recombination at one of three pairs of recombination sites (filled, gray, and open triangles, representing *loxP* sequences) in the ubiquitously expressed *Rosa26*$^{LSL\text{-}Rainbow}$ allele, switching expression from EGFP to one of three other fluorescent proteins indicated. mRNA polyadenylation signal stop cassettes (polyA, hexagons) prevent expression of more than one fluorophore. (B) Logic of Rainbow labeling. After CreER^{T2}-mediated recombination (dashed arrows), each NE cell and all of its daughter cells (short arrows) continuously express one of the other fluorophores. In a cell in which no recombination occurs

(legend continued on next page)

("unrecombined"), EGFP is continuously expressed by the cell and all of its daughters. Although the choice of recombination sites by $CreER^{T2}$ in each cell appears stochastic, slight sequence differences and genomic distances between each *loxP* pair can bias site selection and thus influence the ratio of the three possible recombination outcomes. (C) Optical section of a representative tamoxifen-induced (two 5mg i.p. injections as in Figure 1A), Rainbow-labeled NEB. Individual NE cells (dashed outlines, numbered in schematic) were identified by immunostaining for NE marker CGRP (a neuropeptide) and endogenous fluorescence of the three Rainbow Cre-dependent reporters. (D) Distribution of Rainbow fluorophore expression in mock-injured control (Naph −) and naphthalene-injured (Naph +) NEBs one week after 275mg/kg naphthalene administration with daily 200 μg EdU i.p. injections to detect proliferating NE cells (as in Figure 1A). Results are stratified by proliferation status: all NE ($CGRP^+$) cells, or only EdU^+ NE cells, as indicated. Note recombination resulting in mCerulean expression is favored over mOrange and mCherry, but fluorophore label has little effect on proliferation after injury. n, NE cells scored (control, 23 NEBs, 2 mice; naph, 26 NEBs, 3 mice; same mice and NEBs as Figures 1A–1H). (E) Box-and-whisker plots showing quantification of all NE ($CGRP^+$) and EdU^+ NE cells per NEB in mock-injured control and naphthalene-injured NEBs one week after injury. Individual values (red dots) corresponding to the same NEB are connected by red lines. Median values (left to right), 23, 0, 28, 8 cells. n, NEBs scored (from D); *p = 0.02, two-sided Mann-Whitney *U* test. (F) Empirically determined range of possible proliferative NE cells per NEB, calculated from the naphthalene injury data in Figures 1A–1D. The inferred minimum for each of the 26 scored NEBs (ID 24-49) is the number of distinct Rainbow fluorophores observed in the NEB (EGFP, mCerulean, mOrange, mCherry) with at least one EdU^+ cell (thus 0-4). The inferred maximum is half the total number of EdU^+ NE cells present (rounding down), regardless of Rainbow identity. All values in this range were considered equally likely to represent the true number of NE^{stem} present in that NEB for calculating the empirical distribution in Figure 1H. (G) Outline of NE cell dynamics simulation of NE^{stem} proliferation in NEBs using a custom MATLAB algorithm (STAR Methods). The 5x5 grid represents a NEB, with squares representing each of its initial 25 NE cells. Colored squares indicate Rainbow fluorophore labeling of each cell, white dots show EdU incorporation, and horizontal and vertical subdivisions within squares represent cell division. p, q, r, and T are the free parameters in the simulation. (H, I) Three-dimensional surface representations of the sum of squared residuals across parameter space searches for p, the probability that any one NE cell per NEB possesses the ability to proliferate (i.e., is NE^{stem}), versus q, the NE^{stem} cell division rate per hour (H), or versus T, the total time duration of the simulation in hours (I). Best fits: p = 0.17, $q = 0.0003\ hr^{-1}$, $T = 45$ hr, though note weak dependence on T. Surface color is a visual aid representing surface height. (J) Relative frequency distributions showing the percent of NE cells of each Rainbow fluorophore in the NEB that are EdU^+ at T hours after simulation initiation (dotted lines), compared to the analogous empirical distributions at one week after naphthalene injury *in vivo* (solid lines). These distributions were used to calculate error of fit in parameter space searches. Note that the optimal parameters shown (p = 0.17, $q = 0.0003\ hr^{-1}$, $r = 0.8$, $T = 45$ hr) produce excellent fits for all four Rainbow fluorophores. (K, L) Simulation results (with optimal parameters) showing distributions of (K) the number of cell divisions each proliferative NE cell (NE^{stem}) clone has undergone, and (L) the number of NE cells present in the NEB (red dotted line) compared to the empirical values one week after naphthalene injury in (E) (black solid line). n = 2,779 NE^{stem} cell simulations. Note that the simulation performed well in (L) even though this criterion was not included in the parameter space searches. (M) Scheme for independent tracing of NE cell proliferation after sequential airway injuries using Ki67 instead of BrdU after the second injury. Nucleoside analog EdU (green) traces proliferation after the first round of naphthalene (Naph) injury, and Ki67 immunostaining (red) is used to identify actively proliferating cells 3 days after the second round. (N) Optical section of a NEB (NEB66 Table S2) sequentially injured as above then analyzed by immunostaining for CGRP and Ki67 and click chemistry to detect EdU. White dashed outlines, individual NE cells (numbered in schematic) identified by CGRP immunostaining; arrowheads, EdU^+ (green), $Ki67^+$ (red), and EdU^+ $Ki67^+$ NE cells (yellow); asterisks, EdU^+ or $Ki67^+$ non-NE cells. Note that both NE cells that were proliferating following the second injury (red arrowheads, cells 1 and 3 in schematic) had also proliferated following the first. (O) Quantification of (N) showing distribution of EdU^+ (green), $Ki67^+$ (red), double-positive (yellow), and double-negative (white) $CGRP^+$ NE cells. n, NE cells scored, 13 NEBs, 2 mice. (P) Fraction of NE cells detected proliferating after the second naphthalene injury ($Ki67^+$) stratified by whether cells proliferated after the first injury (EdU^+). n, NE cells scored; ***$p < 10^{-3}$, hypergeometric test of EdU/Ki67 overlap in (O). (Q) Comparison of the fraction of NE cells that proliferated after the first naphthalene injury (cumulative EdU^+ incorporation) with the fraction of actively proliferating cells detected after the second injury ($Ki67^+$ immunostaining). n, NE cells scored. Note the greatly increased likelihood (5-fold) of detecting a NE cell proliferating in the second round if it also proliferated in the first (as also observed by cumulative proliferation detection with BrdU after the second injury in Figure 1L), even though the efficiency of detecting proliferating cells by Ki67 immunostaining (which detects only actively dividing cells) was 70% lower than the cumulative detection of proliferating cells with BrdU over a seven day period (compare (Q) (5% NE cells $Ki67^+$) to Figure 1M (17% NE cells $BrdU^+$), controlling for acquired naphthalene resistance in both cases). Bars, 10 μm.

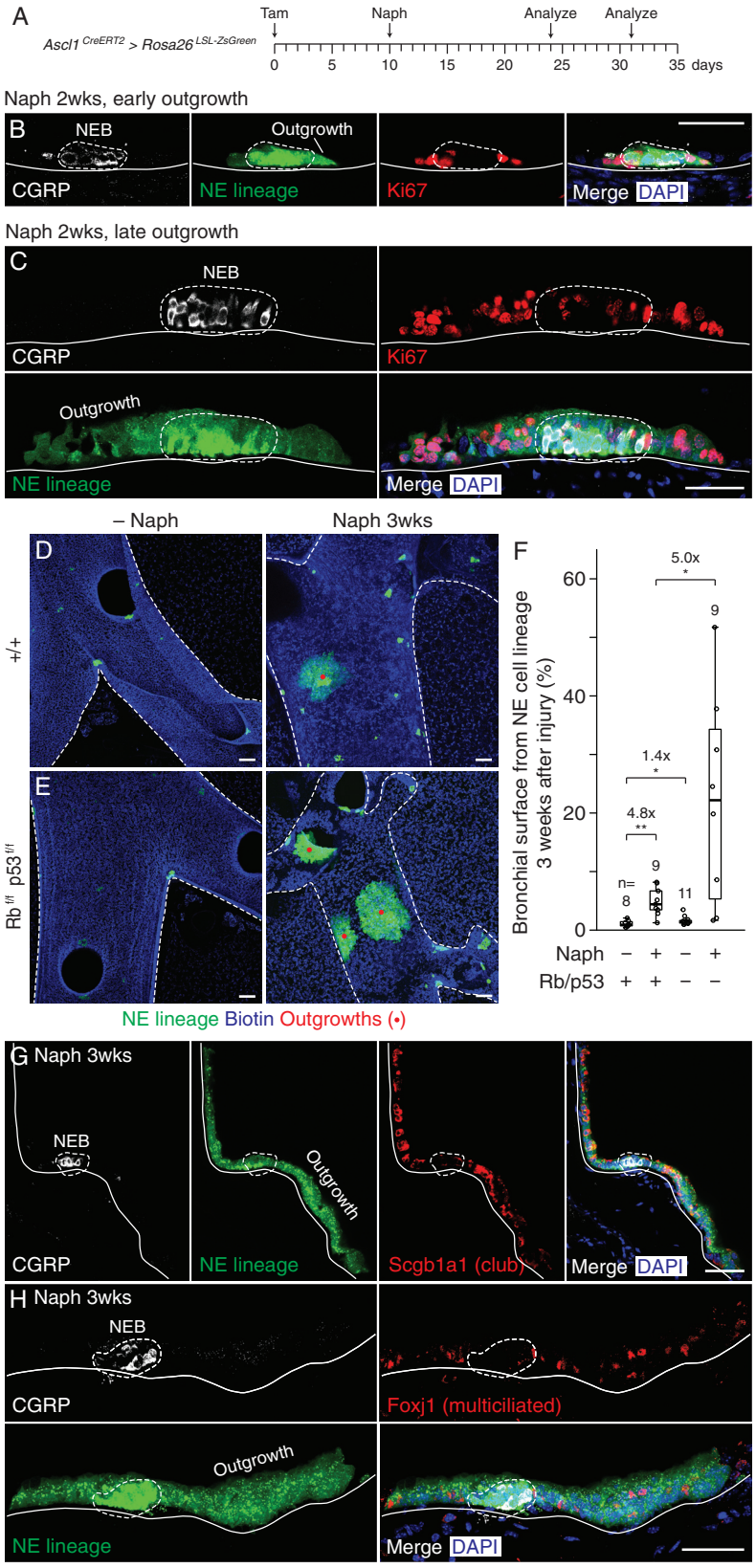

(legend on next page)

Figure S2. NE Outgrowths Are Proliferative and Regenerate Club and Multiciliated Cells, Related to Figures 3 and 6

(A) Scheme for assessing regeneration of bronchial epithelium by NE-derived outgrowths after airway injury. NE cells were lineage-labeled with ZsGreen by tamoxifen induction (4mg, i.p.) of *Ascl1*^{CreERT2}*; Rosa26*$^{LSL\text{-}ZsGreen}$, then airways were injured with naphthalene and analyzed 2 weeks (when repair is ongoing) or 3 weeks later (when repair is nearly complete) by immunostaining as indicated for NE (CGRP), proliferation (Ki67), club (Scgb1a1), and multiciliated (Foxj1) cell markers. (B, C) CGRP$^+$ NEBs (dashed outlines) and associated ZsGreen$^+$ NE lineage-labeled outgrowths ("NE lineage") 2 weeks after injury immunostained for Ki67 to detect actively proliferating cells and counterstained with DAPI. Note that post-deprogramming early (B) and late (C) outgrowths (flanking NEB on both sides) are highly proliferative, whereas NE proliferation has ceased at this time point (Ki67$^+$ cells within the NEB do not colocalize with CGRP and thus are likely NE-derived transitamplifying cells). (D, E) Bronchial branches (dashed outlines) showing lineage-labeled NE cells (ZsGreen, "NE lineage") in wild-type control (D) and Rb/p53-deficient NEBs (E, see Figure 6) after mock injury (− Naph) or 3 weeks after naphthalene injury (Naph 3wks), with biotin counterstain of airway epithelium (blue) and CUBIC clearing. Note that NE deprogramming 1 week after injury (see Figure 3) generates large, lineage-labeled outgrowths (red dots) surrounding the NEB 2 weeks later (D), and outgrowths are larger and more frequent after Rb/p53 deletion (E). (F) Quantification of (D, E) showing the fraction of bronchial surface area covered by wild-type or Rb/p53-deficient NEBs and their outgrowths (cumulatively, NE cell lineage) before and 3 weeks after injury. Note that outgrowth after injury increases NE lineage coverage of the bronchial epithelium ~5-fold in wild-type NEBs, and Rb/p53 deletion results in an additional 5-fold increase. Median values (left to right), 1%, 4%, 1%, 22%; n, fields scored, 2-5 mice per condition (same mice as Figures 6A–6H and 6N–6S); $^{**}p < 10^{-2}$, $^{*}p = 0.08$, two-sided Mann-Whitney *U* tests with Benjamini-Hochberg multiple comparison adjustment. (G, H) NEBs and associated outgrowths 3 weeks after injury immunostained for Scgb1a1 (G, club cell marker) or Foxj1 (H, multiciliated cell marker) and counterstained with DAPI. Note mature outgrowths include both club cells (Scgb1a1$^+$) and multiciliated cells (Foxj1$^+$), indicating complete NE reprogramming to other bronchial fates. Bars, 50 μm (B, C, G, and H), 100 μm (D and E).

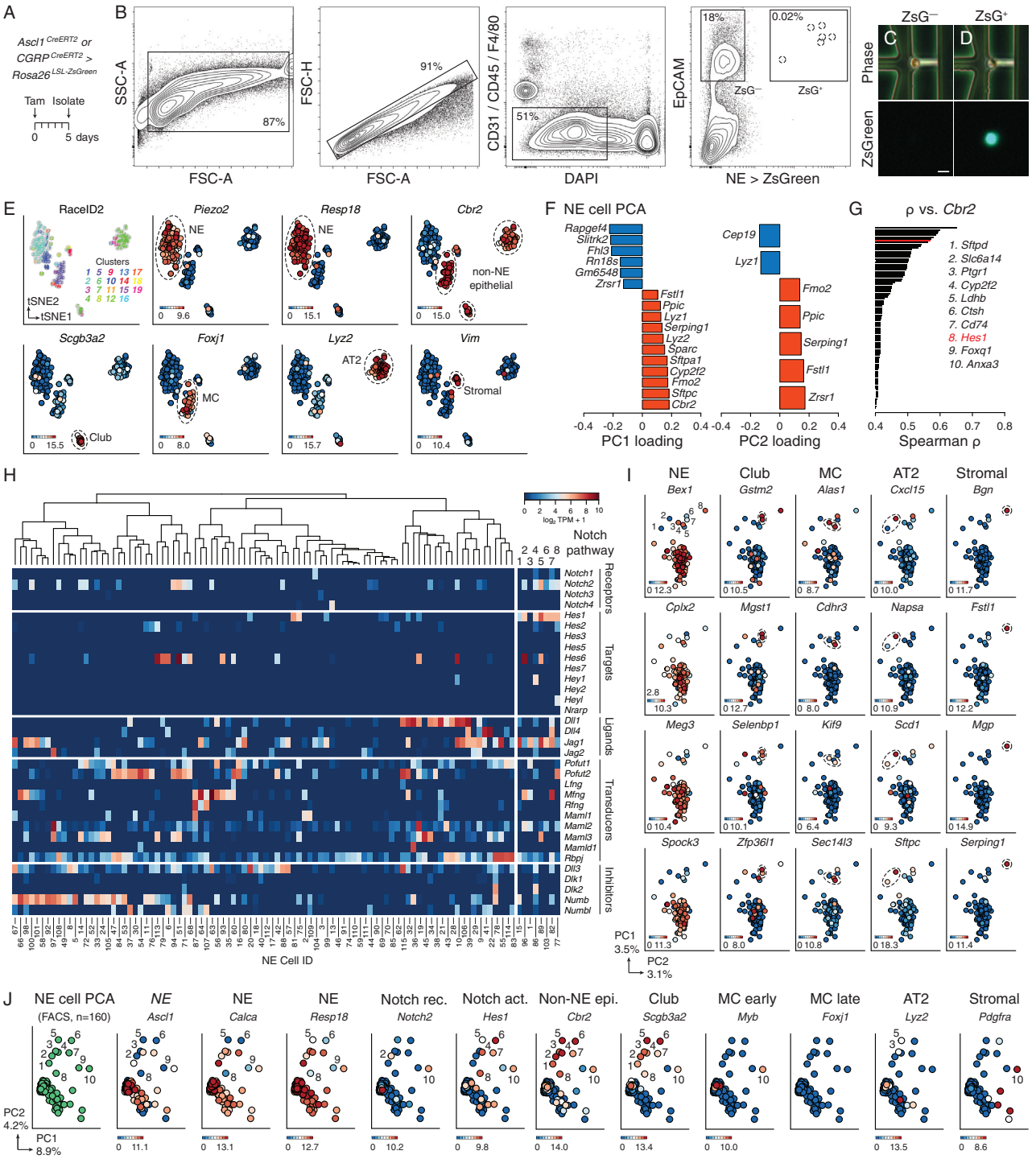

Figure S3. scRNA-Seq of Pulmonary NE and Other Adult Lung Cells after Single Cell Capture by Microfluidics (Fluidigm C_1) or FACS, Related to Figure 4

(A) Scheme for genetic labeling and isolation of NE cells from lungs of *Ascl1*^{CreERT2}*; Rosa26*$^{LSL\text{-}ZsGreen}$ *or CGRP*^{CreERT2}*; Rosa26*$^{LSL\text{-}ZsGreen}$ adult mice 5 days after tamoxifen administration (4mg, i.p.) to induce NE labeling. (B) Sequential FACS gating to isolate lineage-labeled NE cells (DAPI$^-$ CD31$^-$ CD45$^-$ F4/80$^-$ EpCAM$^+$ ZsGreen$^+$) and non-NE epithelial control cells (DAPI$^-$ CD31$^-$ CD45$^-$ F4/80$^-$ EpCAM$^+$ ZsGreen$^-$) following lung dissociation, red blood cell lysis, magnetic depletion of leukocytes and endothelial cells, and fluorescent immunostaining for indicated antigens. SSC, side scatter; FSC, forward scatter; FSC-H, forward scatter pulse height; FSC-H, forward scatter pulse area; CD31 (Pecam1), endothelial marker; CD45 (Ptprc), leukocyte marker; F4/80 (Adgre1, Emr1), macrophage marker; EpCAM, epithelial cell adhesion molecule; NE > ZsGreen, NE cell lineage label ("NE" signifies either *Ascl1*^{CreERT2} or *CGRP*^{CreERT2}). (C, D) Phase contrast (upper)

(legend continued on next page)

and green fluorescence (lower) images of (C) a control non-NE cell (EpCAM$^+$ ZsGreen$^-$) or (D) a NE cell (EpCAM$^+$ ZsGreen$^+$) sorted as in (B) then captured on a Fluidigm C_1 integrated fluidic circuit (medium size, 10-17μm). Images were acquired immediately prior to cell lysis. Bar, 10 μm. (E) scRNA-seq analysis of 225 captured adult lung cells that passed quality controls (including both NE lineage-labeled and control non-NE cells, each cell represented by a colored dot). Cells are plotted using tSNE (t-distributed Stochastic Neighbor Embedding) to represent their full gene expression profiles in two dimensions, and are colored and numbered according to the final cell clustering output by RaceID2 (including outlier identification). Other panels show expression levels for each cell of markers indicated, used in annotation of the five principal cell clusters. For simplicity, the 19 RaceID2-assigned clusters indicated were collapsed to 5 clusters representing known pulmonary cell types: neuroendocrine (NE, identified by *Ascl1*^{CreERT2} or *CGRP*^{CreERT2} lineage label and shown here by *Piezo2* expression), club (identified by *Agr2*, *Aox3*, *Chad*, *Cldn10*, *Cyp2f2*, *Fmo3*, *Gabrp*, *Hp*, *Lrrc26*, *Pon1*, *Reg3g*, *Scgb1a1*, and *Scgb3a2* expression, shown by *Scgb3a2*) multiciliated (MC, identified by *Ccdc39*, *Efhc1*, *Foxj1*, *Myb*, *Rfx2*, *Rfx3*, and *Trp73* expression, shown by *Foxj1*), alveolar type 2 (AT2, identified by *Abca3*, *Etv5*, *Lyz2*, *Muc1*, *Sftpa1*, *Sftpb*, *Sftpb*, and *Sftpd* expression, shown by *Lyz2*), and stromal (identified by *Pdgfra*, *Pdgfrb*, *Tbx4*, *Twist2*, *Eln*, *Fn1*, and *Vim* expression, shown by *Vim*). *Resp18* and *Cbr2* are identified as sensitive and specific NE and non-NE pan-epithelial markers, respectively. Gene expression range (units $\log_2$ TPM+1) for each marker is shown at bottom left and cells are plotted with overlapping points in ascending expression order. (F) Identities and loadings of significant genes (determined by jackstraw software package) in principal components 1 (PC1) and 2 (PC2) after principal component analysis (PCA) of gene expression diversity within 100 lineage-labeled single NE cells. Note that *Cbr2* and other non-NE markers indicative of various cell types are strongly loaded in PC1, suggesting a transcriptional signature of NE lineage reprogramming. (G) Ranked Spearman correlation (ρ) of all expressed genes within NE cells against *Cbr2*, showing the top 100 out of 24,173 queried. The top 10 genes are listed, with *Hes1* (indicative of Notch pathway activity) highlighted in red. (H) Expression heatmap of Notch pathway genes (rows) in individual NE cells (columns). Putative Notch-active NE cells (transitional cells 1-8, selected by visual inspection of NE cell PCA output in Figure 4B) are shown at right and not included in hierarchical clustering applied to the other 92 NE cells. Note that expression of the Notch pathway reporter *Hes1* is sensitive and specific for the 8 transitional cells, but *Notch2* receptor expression includes both Notch-active (*Hes1*-expressing) and Notch-inactive (*Hes1* expression low or off) NE cells. *Hes6* is a direct transcriptional target of Ascl1 (Wapinski et al., 2013). The identification number of each NE cell (see Table S3) is given at bottom. (I) PCA representation of NE cells showing expression (units $\log_2$ TPM+1, range shown at bottom left of each plot) of NE markers (first column) and markers for club (second), multiciliated (MC, third), alveolar type 2 (AT2, fourth) and pulmonary stromal cells (fifth). Cells are plotted in ascending expression order for each gene. Transitional cells 1-8 are numbered in the top left panel, and dashed circles indicate the subset transitioning to the pulmonary cell identity indicated by the column title. (J) PCA of 160 additional NE expression profiles from scRNA-seq of FACS-purified *Ascl1*^{CreERT2}*; Rosa26*$^{LSL\text{-}ZsGreen}$ lineage-labeled adult lung cells. Left panel shows percent of total variance explained by PC1 and PC2, and right panels are color-coded heatmaps showing gene expression levels in each cell of the indicated marker genes of the cell type or pathway shown above gene name. Expression scales, $\log_2$ CPM+1 for ranges indicated. Note most of the 10 transitional cells (numbered) express Notch target *Hes1* and some express *Notch2*, and most show diminished NE markers and enrichment in non-NE markers (club, MC early/late, AT2, or stromal), similar to the 8 NE transitional cells obtained by microfluidic capture (above and Figure 4).

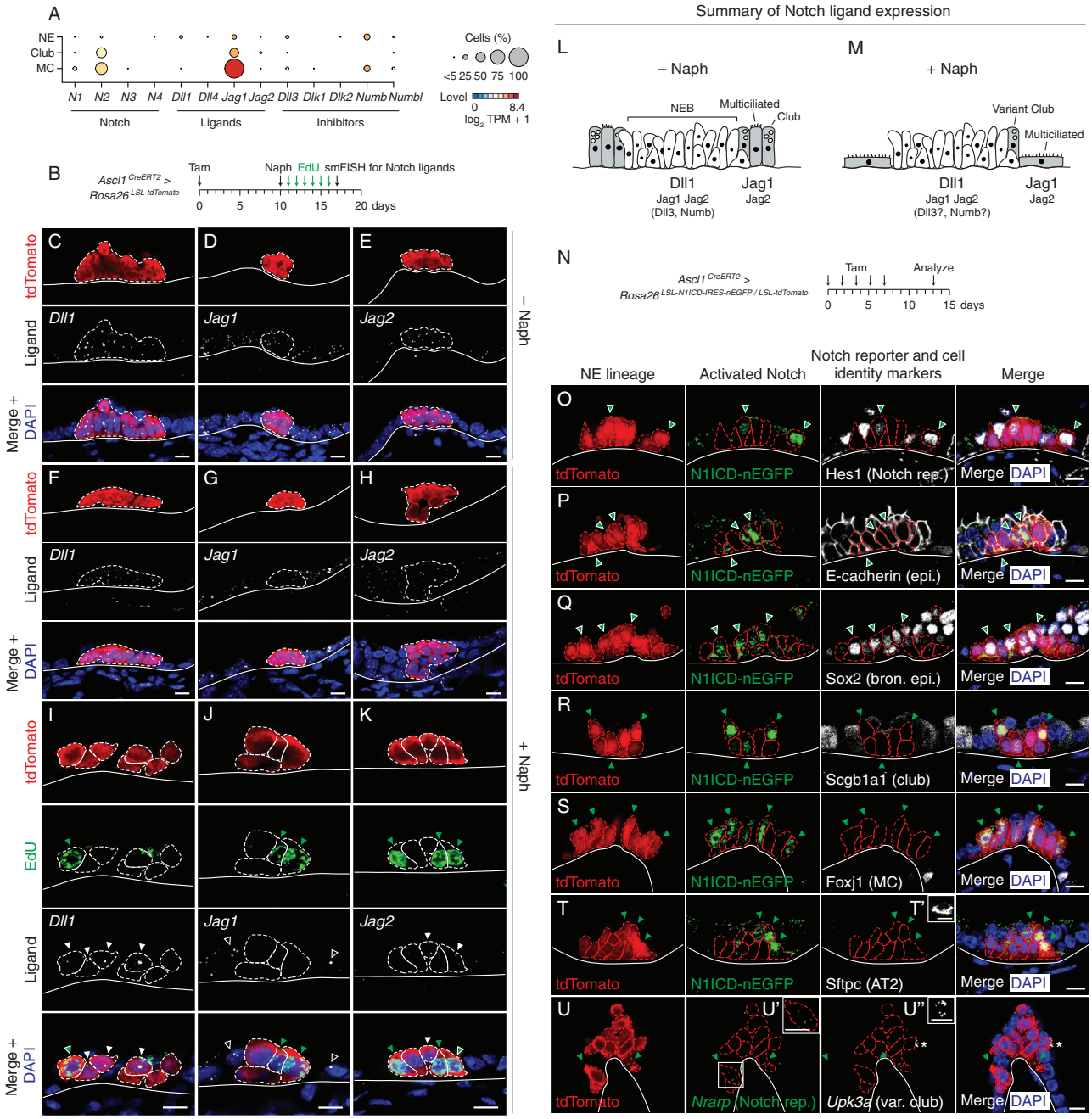

Figure S4. Notch Ligand Expression and Effects of Ectopic Notch Pathway Activation in NEBs, Related to Figure 5

(A) Dot plot showing Notch receptor, ligand, and inhibitor expression in NE (n = 92), club (n = 17), and multiciliated (MC, n = 43) cells from the microfluidic scRNA-seq expression profiles (Figures 4 and S3A–S3I). The 8 Notch-active NE transitional cells are excluded. Dot color, heatmap showing mean gene expression level (log_2 mean TPM+1) of the indicated genes in expressing cells (TPM > 10) of the indicated cell types. Dot size, percent of cells of each type expressing the gene (TPM > 10). Blanks are genes with no detected expression. Note that at least three Notch ligand genes (*Dll1, Jag1, Jag2*) are expressed in NE cells and the two major cell types that surround them, and that NE cells also express Notch inhibitor genes *Dll3*, *Numb*, and *Numblike*. (B) Scheme for assessing spatial expression pattern of Notch ligands by RNAscope single molecule fluorescence *in situ* hybridization (smFISH). Adult *Ascl1*^{CreERT2}*; Rosa26*$^{LSL\text{-}tdTomato}$ mice were treated with tamoxifen (4mg, i.p.) to lineage label NE cells with tdTomato. Ten days later mice were mock- (C-E) or naphthalene-injured (F-K), then treated daily with EdU before analyzing lungs by smFISH for *Dll1* (C, F, I), *Jag1* (D, G, J), and *Jag2* (E, H, K), tdTomato immunostaining for NE cells (C-K), click chemistry for EdU to detect proliferative NE cells (NE^{stem}) (I-K), and DAPI nuclear counterstain (C-K). Data shown are from 1 (control) and 2 (naph) mice. (C-E) Maximum intensity projections of NEBs and adjacent bronchial epithelia from mock-injured lungs. Note that expression of multiple ligand genes are detected (white puncta are amplified signal from individual mRNA molecules), either within the NEB (*Dll1* at high levels, *Jag1* and *Jag2* low) or nearby in club and/or multiciliated cells (*Jag1* high, *Jag2* low). (F-H) Maximum intensity projections as above of naphthalene-injured lungs. Expression patterns for all three ligands are similar to those of mock-injured controls.

(legend continued on next page)

(I-K) Optical sections of NEBs showing that EdU$^+$ NE cells (NE^{stem}, green arrowheads) and neighboring NE and non-NE epithelial cells express mRNA for Notch ligands, so could provide the Notch-activating signal following injury. White arrowheads, ligand-expressing NE cells (e.g., *Dll1*, *Jag2*); white open arrowheads, ligand-expressing non-NE cells (e.g., *Jag1*). (L, M) Diagrams summarizing above Notch ligand and inhibitor expression in NEBs (white) and adjacent club and multiciliated cells (gray) before (L, – Naph) and one week after (M, + Naph) naphthalene injury. The inhibitors might prevent Notch pathway activation prior to injury. (N-U) Notch pathway activation in NE cells *in vivo* by a constitutively active Notch is not sufficient for full reprogramming to other pulmonary fates. (N) Adult mice of genotype indicated were treated with five doses of tamoxifen (4mg, i.p.), permanently inducing a constitutively active Notch receptor fragment (N1ICD) and nuclear-localized green fluorophore (nEGFP), as well as cytoplasmic fluorescent lineage tag (tdTomato) in adult Ascl1$^+$ NE cells. One week later, lungs were analyzed by immunostaining (O-T) or RNAscope smFISH (U) for Notch reporters and cell type-specific markers to assess NE reprogramming to other cell fates. (O-T) Optical sections of NEBs treated as above analyzed for tdTomato (NE lineage, ~100% NE cells, red dashed outlines) and immunostained for nEGFP (cells expressing the constitutively active Notch, ~40% NE cells due to inefficient recombination), Notch pathway reporter Hes1 (O), epithelial marker E-cadherin (P), bronchial epithelial marker Sox2 (Q), club cell marker Scgb1a1 (R), multiciliated cell (MC) marker Foxj1 (S), and alveolar type 2 (AT2) marker Sftpc (T), counterstained with DAPI. Inset T', close-up of nearby Sftpc-expressing AT2 cell as a positive control. (U) smFISH for *Nrarp* (indicating Notch activation) and *Upk3a* (variant club cell marker), with tdTomato immunostaining and DAPI nuclear counterstain as above. Green and white puncta, amplified signal from individual mRNA molecules (see close-ups of boxed *Nrarp*-expressing NE cell in inset U' and nearby *Upk3a*-expressing variant club as a positive control in inset U''). Green arrowheads (O-U), NE lineage-labeled cells (tdTomato$^+$) showing Notch activation; outlined arrowheads (O-U), Notch-activated cells also expressing the indicated cell identity marker; asterisk (U), portion of a neighboring non-NE *Upk3a*$^+$ (variant club) cell. Note that Notch-activated NE cells express Hes1 and *Nrarp* and maintain expression of E-cadherin and Sox2, but do not express club, variant club, multiciliated, or alveolar type 2 markers. Data from 4 mice used in Figures 5K–5M (O-T) and 2 additional mice treated identically (U). Bars, 10 μm.

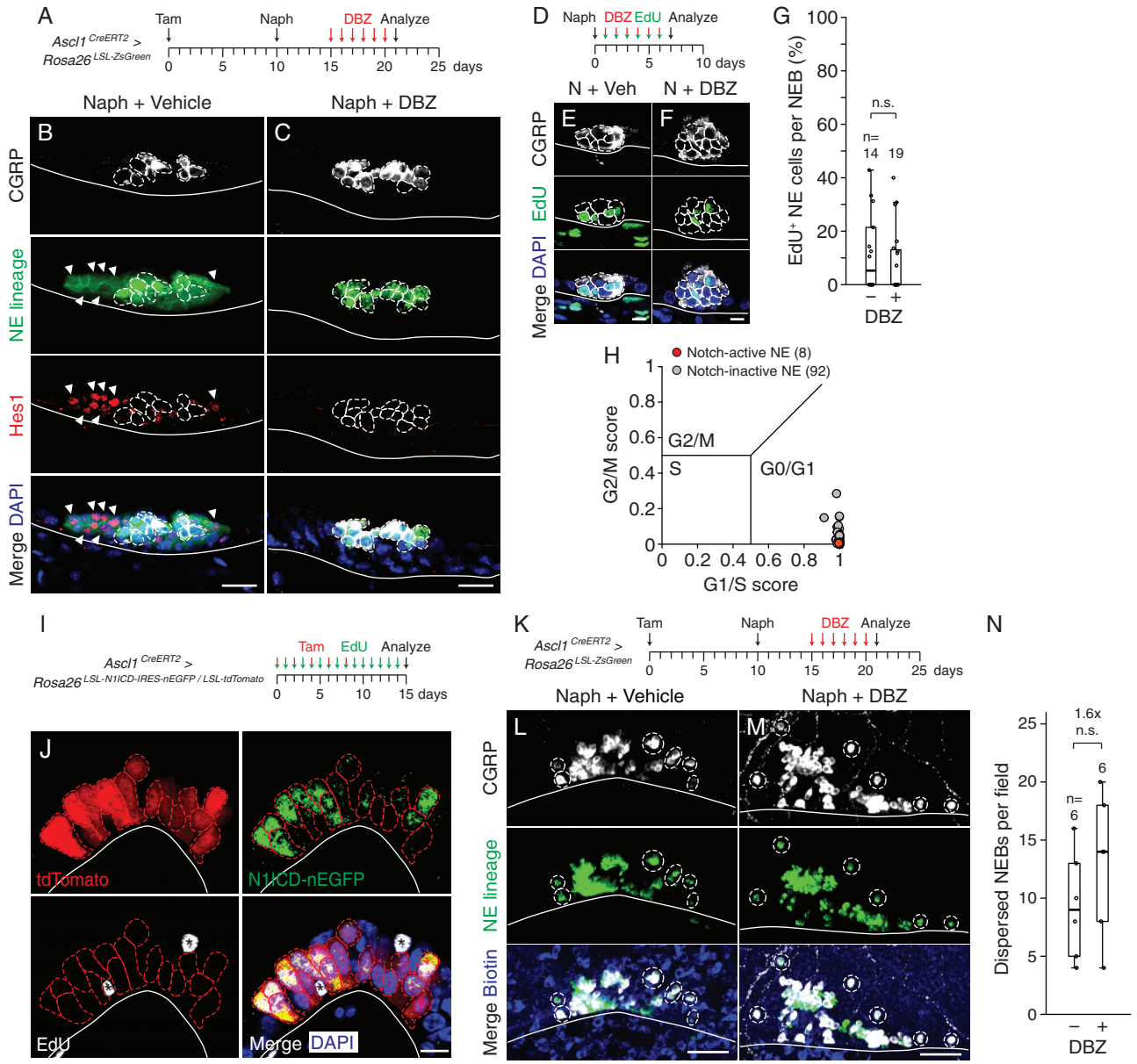

Figure S5. Notch Inhibition after Naphthalene Injury Prevents Outgrowth Formation but Is Dispensable for NE Proliferation and Dispersal, Related to Figure 5

(A) Scheme for assessing Notch pathway requirement in NE cell outgrowth from NEBs after airway injury. Adult *Ascl1*^{CreERT2}*; Rosa26*$^{LSL\text{-}ZsGreen}$ mice were treated with tamoxifen (4mg, i.p.) to lineage label NE cells, then ten days later treated with naphthalene to injure airways. Naphthalene-injured mice were treated with DBZ daily during the NE deprogramming period (days 5-10 after injury) and NE cell outgrowth from NEBs was analyzed at day 11. (B, C) NEBs from control vehicle-treated (B) or DBZ-treated (C) mice as above analyzed for ZsGreen ("NE lineage") and immunostained for NE marker CGRP and Notch pathway reporter Hes1, counterstained with DAPI. Note that outgrowth from the NEB (indicating prior productive deprogramming) and Notch pathway activation (nuclear Hes1 expression) in NE lineage-labeled cells (arrowheads) are evident in vehicle control but absent after DBZ treatment. Data from mice in Figure 5G-J. (D) Scheme for assessing Notch pathway requirement for NE proliferation after airway injury. After naphthalene injury of adult mice, Notch inhibitor DBZ was injected daily along with EdU to track cell division during the NE proliferation period (days 1-6 after injury), and proliferation analyzed at day 7. (E, F) NEBs from mice as above treated with vehicle (E) or DBZ (F) and analyzed by immunostaining for NE marker CGRP, click chemistry to detect EdU, and DAPI counterstain. (G) Quantification of (E, F) showing percent of NE cells per NEB labeled with EdU. Median values, 5% (vehicle), 0% (DBZ); n, NEBs scored, 2 mice per condition; p = 0.5, two-sided Mann-Whitney *U* test. Note that DBZ does not significantly alter NE proliferation, although proliferation in both conditions is reduced relative to standard conditions (compare with Figure 1D), presumably due to non-specific effects of the DBZ vehicle. (H) Cyclone computational cell cycle phase assignment of NE cells from microfluidic scRNA-seq gene expression profiles (Figures 4 and S3A–S3I). Red dots, results from the 8 Notch-active NE transitional cells; gray dots, results for the 92 other (Notch-inactive) NE cells. Note that both Notch-active and other NE cells are assigned to G0/G1 phase. (I) Scheme for assessing NE proliferation after ectopic Notch pathway activation. Adult mice of the genotype indicated were treated with five doses of tamoxifen (4mg, i.p.) as shown, permanently inducing a

(legend continued on next page)

constitutively active Notch receptor fragment (N1ICD) and nuclear-localized green fluorophore (nEGFP), as well as a cytoplasmic fluorescent lineage tag (tdTomato) in Ascl1$^+$ adult NE cells. EdU was injected daily throughout to track cell division until analysis on day 7. (J) Optical section of a NEB from mice treated as above analyzed for tdTomato (NE lineage, ~100% NE cells, red dashed outlines), nEGFP by immunostaining (cells expressing the constitutively active Notch, ~40% NE cells), EdU by click chemistry, counterstained with DAPI. Note that none of the 10 Notch-activated NE cells (tdTomato$^+$ nEGFP$^+$) have proliferated (all are EdU$^-$), nor have any of the Notch-inactive NE cells (tdTomato$^+$ nEGFP$^-$) within the same NEB. NE cells are also tightly packed and do not exhibit migratory morphologies, indicating Notch activation does not induce dispersal. Asterisks, EdU$^+$ tdTomato$^-$ cells. The same results obtained for all 300 NE cells scored in 13 NEBs from 2 mice. (K) Scheme for assessing Notch pathway requirement for NE dispersal following airway injury. Adult *Ascl1^{CreERT2}; Rosa26$^{LSL\text{-}ZsGreen}$* mice were treated with tamoxifen (4mg, i.p.) to lineage label NE cells, then administered naphthalene to injure airways. Naphthalene-injured mice were treated with Notch inhibitor DBZ daily during the NE deprogramming period (days 5-10 after injury) and NE cell dispersal from NEBs was analyzed at day 11. (L, M) NEBs from mice as above treated with vehicle (L) or DBZ (M) analyzed for ZsGreen ("NE lineage") and immunostained for NE marker CGRP, counterstained for biotin. Note similar number and distribution of dispersed NE satellite cells (dashed outlines) in both conditions. (N) Quantification of NEB dispersal in (L, M). Median values, 9 (vehicle), 14 cells (DBZ); n, fields scored, 3 mice per condition (same mice as (A-C) and Figures 5G–5J); p = 0.3, two-sided Mann-Whitney *U* test. Bars, 25 μm (B and C), 10 μm (E, F, and J), 50 μm (L and M).

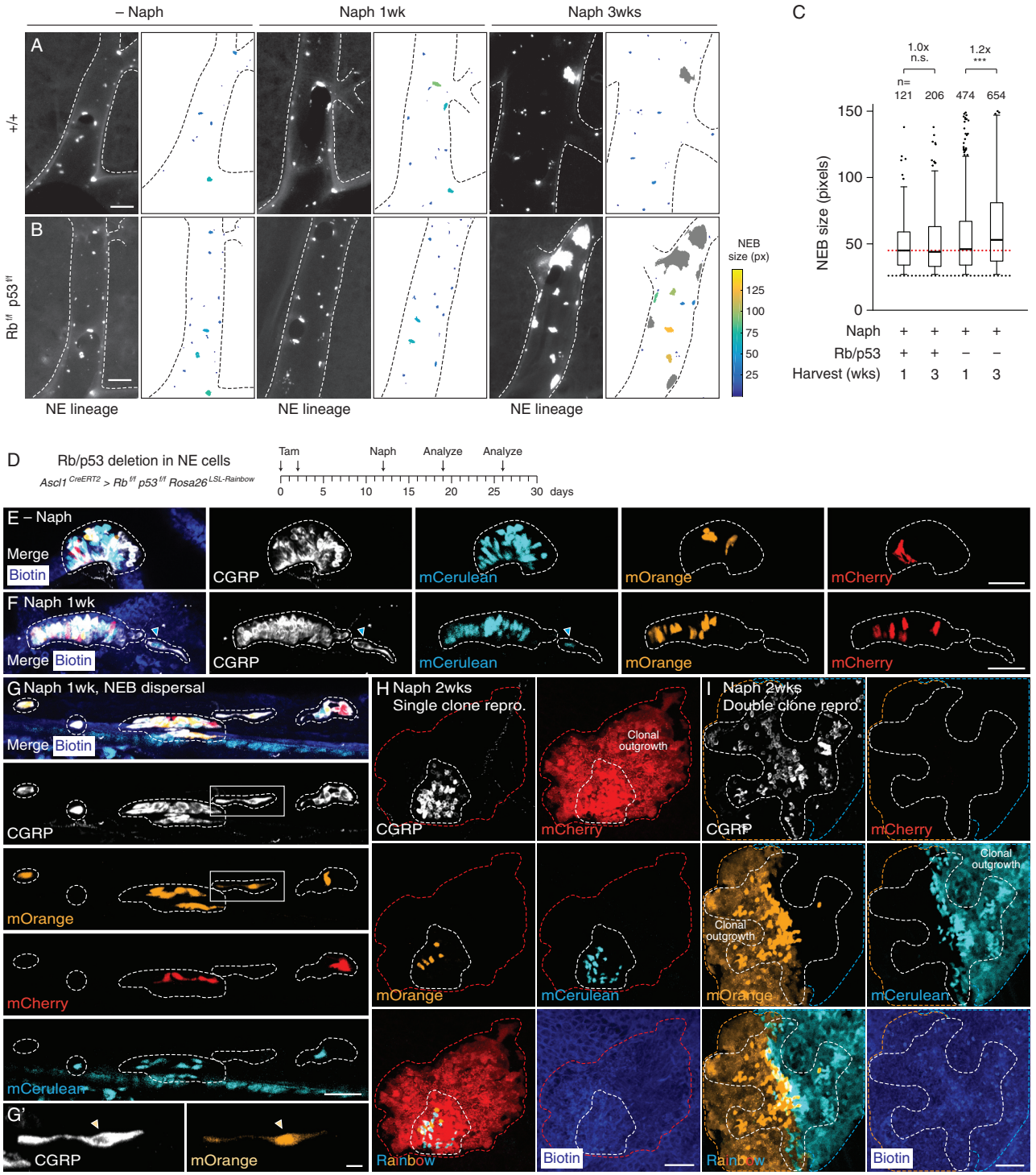

Figure S6. Conditional Deletion of *Rb and p53* Prolongs NE Cell Proliferation after Airway Injury but Does Not Affect Migration Dynamics of Dispersal or Clonality of Deprogramming, Related to Figure 6

(A-C) Effect of Rb/p53 deletion on NE cell proliferation after airway injury, as assessed by NEB size. (A, B) Bronchial branches (dashed outlines) as in Figures 6N–6Q showing lineage-labeled NE cells (ZsGreen, "NE lineage") in wild-type control (A) and Rb/p53-deficient NEBs (B) 1 week after mock injury (– Naph), or 1 (Naph 1wk) or 3 weeks (Naph 3wks) after naphthalene injury. In the paired schematics, ZsGreen fluorescence signal of each NEB has been segmented and color coded by its size in pixels (heatmap scale on right). NEBs > 299 pixels are assumed to be NEBs with outgrowths (Figure 3), and are colored gray and excluded from quantification in (C). (C) Quantification of (A, B) showing NEB size distributions 1 and 3 weeks after naphthalene injury. Note Rb/p53 deletion results in a 15%

(legend continued on next page)

increase in median NEB size 3 weeks after injury (due to sustained NE proliferation), whereas wild-type NEB size is unchanged. Black dotted line, threshold minimum size for NEB identification (26 pixels); red dotted line, median NEB size in wild-type condition 1 week after naphthalene injury. Individual NEB values are shown for outliers (> 1.5x interquartile range). Median values (left to right), 45, 44, 46, 53 pixels; n, NEBs scored in 4 mice per condition (same mice as Figures 6A–6H and 6N–6S); ***$p < 10^{-4}$, two-sided Mann-Whitney *U* tests with Benjamini-Hochberg multiple comparison adjustment. (D) Scheme for tracing cell dynamics and reprogramming of Rb/p53-deficient NE cells at clonal resolution. Adult mice of the genotype shown were induced twice with tamoxifen (5mg, i.p.) to delete conditional *Rb* and *p53* alleles and stochastically label Ascl1$^+$ NE cells with Rainbow reporters. Mice were injured with naphthalene and NE cell distribution and clonal expansion were analyzed 1 and 2 weeks later. (E, F) Rb/p53-deficient Rainbow-labeled NEBs as above from mock-injured control (E, split channels shown to right) or naphthalene-injured mice (F) analyzed 1 week after injury for Rainbow fluorescence (mCerulean, mOrange, mCherry), immunostained for CGRP, and counterstained for biotin. Note NEB dispersal in (F) and the presence of an mCerulean$^+$ NE satellite cell (cyan arrowhead). All Rainbow-labeled cells in (F) remain CGRP$^+$, indicating that deprogramming has not yet occurred. (G) An Rb/p53-deficient NEB 1 week after naphthalene injury showing extreme dispersal and individual CGRP$^+$ NE satellite cells (split channels shown below). White dashed outlines, NEB and its dispersed cells identified by CGRP immunostaining and Rainbow fluorophores. (G') Close-up of boxed region showing a CGRP$^+$ mOrange$^+$ NE satellite cell with migratory morphology resembling developmental NE "slithering" (Kuo and Krasnow, 2015; Noguchi et al., 2015). (H, I) Rb/p53-deficient NEBs 2 weeks after naphthalene administration showing the most common outgrowth pattern (H), in which a single NE clone (mCherry$^+$) reprogrammed and expanded dramatically (as in Figure 3E), or the less common pattern (I) in which two NE cells in the same NEB (mCerulean$^+$ and mOrange$^+$) reprogrammed and clonally expanded, though maintain distinct territories (as in Figure 3F). White dashed outlines, NEB boundaries identified by CGRP immunostaining; colored dashed lines, clone outgrowth boundaries. Bars, 500 μm (A and B), 50 μm (E-I), 10 μm (G').

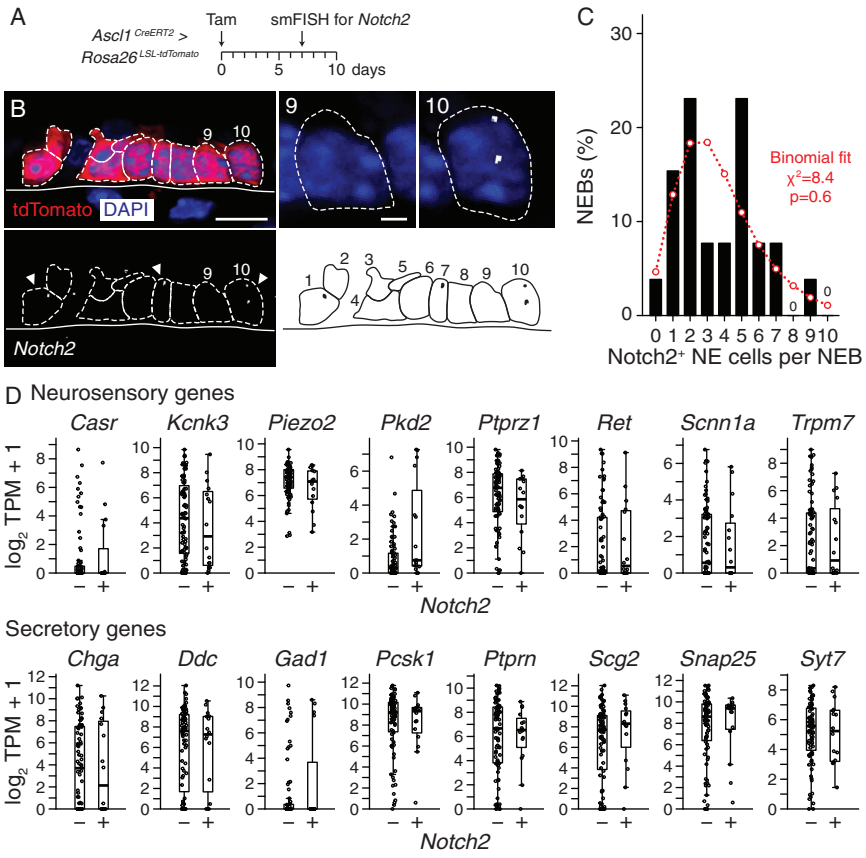

Figure S7. A Subpopulation of Differentiated NE Cells Expresses *Notch2*, Related to Figure 7

(A) Scheme for analyzing pattern of *Notch2* mRNA expression in NE cells *in vivo*. Adult *Ascl1*^{CreERT2}; *Rosa26*$^{LSL\text{-}tdTomato}$ mice were induced with tamoxifen (4mg, i.p.) to label NE cells and analyzed 1 week later by RNAscope smFISH for *Notch2* (white), tdTomato immunostaining of NE cells (red), and DAPI nuclear counterstain (blue). (B) Optical section of a NEB. Close-ups at right show *Notch2*$^{-}$ NE cell (cell 9 in schematic) and *Notch2*$^{+}$ NE cell (cell 10) with amplified signal from individual *Notch2* mRNAs (white puncta in cell 10, black dots in schematic). Note *Notch2*$^{+}$ cells (arrowheads) are scattered around the NEB like NE^{stem}. (C) Quantification of (B) (n = 32 NEBs scored, same NEBs and mice as Figure 7A "– Naph"). Red, binomial fit. Note similar number of *Notch2*$^{+}$ cells as NE^{stem} (~2-4, Figure 1H) in each NEB. (D) Comparison of expression (log_2 TPM+1) of indicated genes involved in NE cell sensory and secretory functions in *Notch2*$^{-}$ ("bulk") NE cells (n = 84) and *Notch2*$^{+}$ NE cells (putative NE^{stem}, n = 16) from microfluidic scRNA-seq (Figures 4 and S3A–S3I). Note similar expression levels, implying that putative NE^{stem} cells have the same physiological functions as "bulk" NE cells. Bars, 10 μm (B), 2 μm (insets).